Buoyancy-Driven Coastal Currents off Oregon during Fall and Winter

Citation	Mazzini, P. L. F., Barth, J. A., Shearman, R. K., & Erofeev, A. (2014). Buoyancy-Driven Coastal Currents off Oregon during Fall and Winter. Journal of Physical Oceanography, 44(11), 2854-2876. doi:10.1175/JPO-D-14-0012.1
DOI	10.1175/JPO-D-14-0012.1
Publisher	American Meteorological Society
Version	Version of Record
Terms of Use	http://cdss.library.oregonstate.edu/sa-termsofuse

Buoyancy-Driven Coastal Currents off Oregon during Fall and Winter

PIERO L. F. MAZZINI, JOHN A. BARTH, R. KIPP SHEARMAN, AND A. EROFEEV

College of Earth, Ocean, and Atmospheric Sciences, Oregon State University, Corvallis, Oregon

(Manuscript received 17 January 2014, in final form 20 July 2014)

ABSTRACT

During fall/winter off the Oregon coast, oceanographic surveys are relatively scarce because of rough weather conditions. This challenge has been overcome by the use of autonomous underwater gliders deployed along the Newport hydrographic line (NH-Line) nearly continuously since 2006. The discharge from the coastal rivers between northern California and the NH-Line reach several thousands of cubic meters per second, and the peaks are comparable to the discharge from the Columbia River. This freshwater input creates cross-shelf density gradients that together with the wind forcing and the large-scale Davidson Current results in strong northward velocities over the shelf. A persistent coastal current during fall/winter, which the authors call the Oregon Coastal Current (OCC), has been revealed by the glider dataset. Based on a two-layer model, the dominant forcing mechanism of the OCC is buoyancy, followed by the Davidson Current and then the wind stress, accounting for 61% (±22.6%), 26% (±18.6%), and 13% (±11.7%) of the alongshore transports, respectively. The OCC average velocities vary from 0.1 to over 0.5 $m\,s^{-1}$, and transports are on average 0.08 (±0.07) Sverdrups (Sv; 1 Sv $\equiv 10^6\,m^3\,s^{-1}$), with the maximum observed value of 0.49 Sv, comparable to the summertime upwelling jet off the Oregon coast. The OCC is a surface-trapped coastal current, and its geometry is highly affected by the wind stress, consistent with Ekman dynamics. The wind stress has an overall small direct contribution to the alongshore transport; however, it plays a primary role in modifying the OCC structure. The OCC is a persistent, key component of the fall/winter shelf dynamics and influences the ocean biogeochemistry off the Oregon coast.

1. Introduction

Buoyancy can be a major forcing mechanism on continental shelves where significant amounts of freshwater enter the ocean, provided by coastal rivers or ice melt (Hill 1998). Buoyancy forcing generates currents that become trapped to the coast, under the effect of the Earth's rotation, and propagate in the same direction as coastal-trapped waves (Chao and Boicourt 1986). These buoyancy-driven currents are commonly referred to as coastal currents. Several examples of coastal currents have been observed around the world, such as the Alaska Coastal Current (Royer 1981), the Norwegian Coastal Current (Mork 1981), and the Delaware Coastal Current (Münchow and Garvine 1993a).

Coastal currents can propagate long distances along the coast as coherent structures and are a primary connection between estuarine environments and the ocean. These currents play a crucial role in the along-shelf transport of freshwater, nutrients, larvae, pollutants, sediment, and so on. At the same time, the cross-shelf transport is inhibited by the formation of sharp density fronts, which act as barriers, blocking exchange processes between the regions inshore of the front and the adjacent ocean waters offshore. The role that these fronts play in the biogeochemistry of the ocean is therefore evident, and they can significantly impact the marine ecosystems (Hickey et al. 2010). Besides controlling the along- and cross-shelf transports, the freshwater has profound effects on continental shelf dynamics by modifying the ocean stratification. These changes in stratification may allow or modify internal motions (e.g., Nash and Moum 2005) and also affect small-scale processes such as turbulence and mixing.

The main goal of this work is to describe in detail, for the first time, coastal currents off the coast of Oregon during the fall and winter seasons, which are extremely challenging to survey due to the rough ocean and weather conditions during that time of the year. By exploiting a new ocean observing technology, underwater gliders, it has become possible to sample the Oregon coastal waters

Corresponding author address: Piero L. F. Mazzini, College of Earth, Ocean, and Atmospheric Sciences, Oregon State University, 104 CEOAS Administration Building, Corvallis, OR 97331-5503.
E-mail: pmazzini@coas.oregonstate.edu

DOI: 10.1175/JPO-D-14-0012.1

during these seasons. This work focuses on the description of the main characteristics of the coastal currents, their response to wind forcing, and also provide estimates of both the freshwater and total northward transports, as well as the seasonal variability of the freshwater content, observed off the central Oregon coast.

The remainder of this introduction describes the regional setting and summarizes coastal current dynamics. The following sections of the paper consist of data and methodology, results, discussion, and, finally, the conclusions.

a. Regional setting

Over the course of a year, a remarkable contrast of forcing mechanisms, as well as stratification and circulation, takes place off the Oregon coast (and U.S. Pacific Northwest). Two distinct oceanographic regimes are clearly observed: the fall and winter seasons and the spring and summer seasons (Huyer et al. 1975; Huyer 1977).

A number of observational studies addressing aspects of continental shelf dynamics have been conducted off the Oregon coast and U.S. Pacific Northwest during spring and summer seasons (e.g., Barth and Wheeler 2005). During fall and winter on the other hand, oceanographic surveys are relatively scarce, which results from the difficulties in surveying the shelf, mainly due to the rough ocean conditions produced by the passage of synoptic cold fronts and strong winds associated with them during that time of the year.

Since 2006, the Glider Research Group at Oregon State University (OSU) has used autonomous underwater gliders to survey the continental shelf and slope along the historical Newport hydrographic line (NH-line; 44.65°N), off the coast of Newport, Oregon (Fig. 1). Since the gliders are autonomous, they allow sampling in all weather conditions, and measurements along the NH-line have been made throughout the year. These glider data provide the largest high-resolution data collection off the Oregon coast up to date.

Off the Oregon coast, during the spring and summer seasons, quasi-steady winds blow toward the south (upwelling favorable), and as a response, freshwater is located offshore of the upwelling front and advected southward (against the direction of buoyancy forcing) from a single large source: the Columbia River (Barnes et al. 1972). A very different scenario is observed during other seasons.

During fall and winter, freshwater is discharged into the coastal ocean from multiple small to medium sized mountainous rivers along the Oregon coast, driven by storm events with high synoptic variability, and once the freshwater encounters the ocean, it becomes susceptible to the action of the wind field, which often blows northward (downwelling favorable). One example of the river discharges influencing the Oregon and northern California coasts is shown in Fig. 1, in a satellite image from the Moderate Resolution Imaging Spectroradiometer (MODIS)/*Terra* on 27 January 2012. The image shows the 555-nm remote sensing reflectance R_{rs} that is a proxy for turbidity in the water column (Thomas and Weatherbee 2006). A coherent alongshore band of turbid waters is present along the coast, with continuous input near river mouths and the individual plumes distorted toward the north, indicating northward propagation. South of the NH-line, the outflow from the

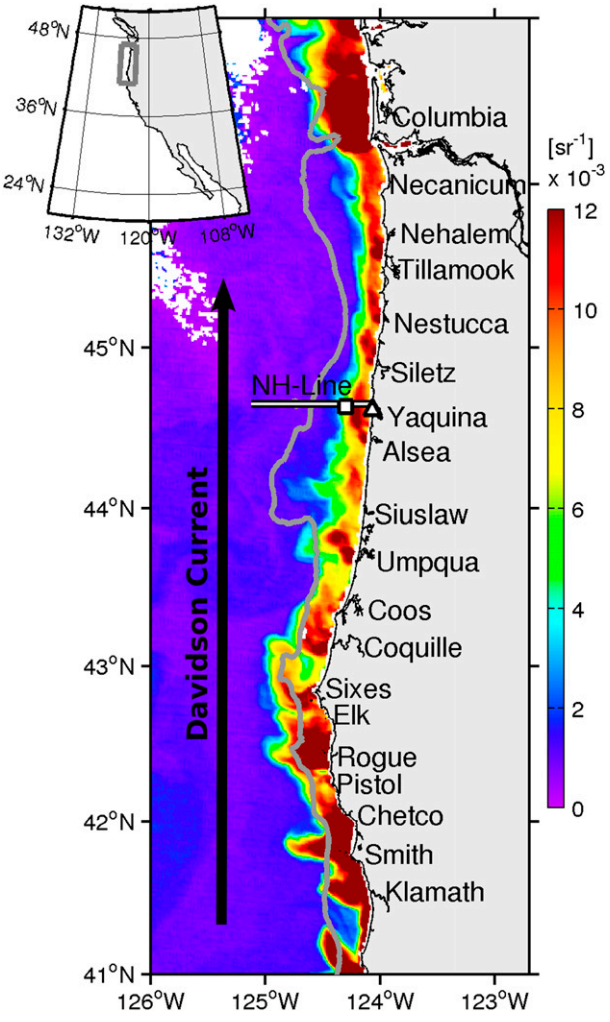

FIG. 1. Snapshot taken from MODIS/*Terra* on 27 Jan 2012 for the 555-nm remote sensing reflectance R_{rs}, an effective tracer of turbidity in the water column (Thomas and Weatherbee 2006). Warm colors are indicators of river plumes and the coastal current along the northwest coast of the United States. The NH-Line, surface buoy NH10 (square), and meteorological station NWPO3 (triangle) are shown on the map, as well as an arrow indicating the Davidson Current. The names of the major rivers along the Oregon and northern California coast are shown. The edge of the continental shelf is indicated by the 200-m isobath in gray.

Yaquina, Alsea, Siuslaw, Umpqua, Coquille, Rogue, and Chetco Rivers in southern and central Oregon and Smith and Klamath Rivers in northern California added up may reach magnitudes above $10\,000\,m^3\,s^{-1}$, becoming comparable to discharges from the Columbia River, which has an average discharge during winter of $7400\,m^3\,s^{-1}$.

The knowledge of oceanographic conditions during winter and fall seasons off the Oregon coast come from a small number of observational studies. Huyer (1977) analyzed salinity profiles along the NH-Line and found that during the winter, low salinities were confined to the station closest to the coast, NH-5 (9 km from the coast, over the 50-m isobath), and not present offshore, which the author attributed to discharge from the coastal rivers. Also, significant stratification was observed at NH-5, while the rest of the shelf showed very weak stratification above the pycnocline, located between 75 and 125 m deep.

Along-shelf currents over the Oregon continental shelf were studied by Huyer et al. (1975, 1978). During winter, the average flow is northward, with no vertical shear (offshore). During spring, the flow is southward in the entire water column, but is intensified at the surface. In summer, the greatest shear occurs, when it is observed that there is a southward flow in the surface and a poleward flow near the bottom. According to Huyer et al. (1978), the shear is in approximate geostrophic balance, except near the bottom due to Ekman veering. The authors also found that low-frequency current fluctuations are correlated with wind stress and sea level at the coast and in all seasons, the fluctuations decrease in the offshore direction, and that they are greater in winter than in summer.

Besides freshwater runoff, another important driving force in the fall–wintertime off the Oregon coast is the wind field, mostly blowing in the northward direction. The response to downwelling-favorable winds off the Oregon coast was studied by Allen and Newberger (1996), using a two-dimensional numerical model with typical bathymetry and stratification off the Oregon coast, but not including river discharge, and forcing with idealized wind. The authors found that as a response to northward wind stress, a downwelling front is formed, which slowly propagates offshore under constant forcing. Inshore of the front, the density is well mixed and the alongshore velocities are small, while offshore of the front an intensified coastal jet is formed, sheared both horizontally and vertically. Austin and Barth (2002a), based on drifter displacements under downwelling-favorable winds, calculated average northward current speeds to be $0.24 \pm 0.08\,m\,s^{-1}$ and a maximum value observed of $1\,m\,s^{-1}$.

It has also been long known that during wintertime off the Pacific Northwest, specifically north of Point Conception (34°N), there is a tendency of the flows to be directed to the north. This large-scale structure is known as the Davidson Current (Jones 1918). The large-scale, cross-shelf density gradients caused by the freshwater runoff plus the northward, downwelling-favorable, along-shelf wind stress, added to the wintertime large-scale Davidson Current, can drive strong northward velocities over the shelf.

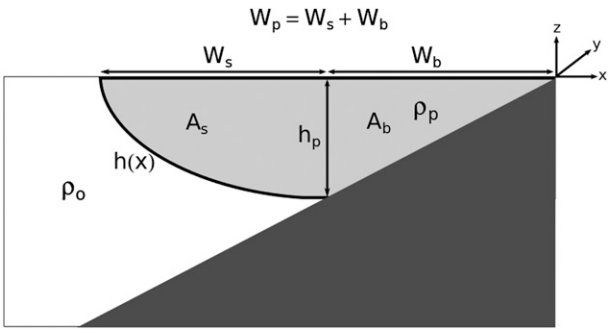

FIG. 2. Cross-section scheme of a buoyant plume, far from the bulge where the river enters the ocean (based on Lentz and Largier 2006). Total width of the plume is $W_p = W_s + W_b$, where W_s is the offshore part of the plume that is not in direct contact with the bottom, with cross-sectional area A_s, and W_b is the nearshore portion of the plume, which is in contact with the bottom, with cross-sectional area A_b. The term ρ_o is the ocean density; ρ_p is the plume density; h_p is the maximum thickness of the plume (where the front intersects the bottom), which separates the parts with and without contact with the bottom; and $h(x)$ is the shape of the front.

b. *Coastal current dynamics*

As freshwater exits from rivers and estuarine environments and enters the coastal ocean, it rotates anticyclonically due to the Coriolis effect (Chao and Boicourt 1986). In the absence of external forcing, two dynamically distinct regions arise: the bulge, near the river mouth, and the coastal current, farther downstream where the flow is confined to the coast (Chao and Boicourt 1986). The bulge is an unsteady, continuously growing feature, where both advection and rotational effects are major terms in the momentum balance, while the coastal current, which is the focus of this work, is a predominantly steady feature characterized by a semigeostrophic balance to first order (away from the bulge and the nose of the coastal current) (e.g., Blanton 1981; Garvine 2004; Yankovsky 2006).

A cross-sectional scheme of a coastal current is shown in Fig. 2, following Lentz and Largier (2006), and can be characterized by a small set of parameters. The total width of the plume is given by $W_p = W_s + W_b$, where W_s is the offshore part of the plume that is not in contact with the bottom, with cross-sectional area A_s, and W_b is the nearshore portion of the plume, which is in direct

contact with the bottom, with cross-sectional area A_b. The ocean density is ρ_o, the plume density is ρ_p, the maximum thickness of the plume is h_p, where the front intersects the bottom and that separates the parts with and without contact with the bottom, and $h(x)$ is the shape of the front.

Chapman and Lentz (1994) classified coastal currents as being surface trapped or bottom advected. Coastal currents are considered surface trapped when $A_s \gg A_b$, with their dynamics highly influenced by wind forcing and ambient currents. Now, when $A_s \ll A_b$, the coastal current is classified as bottom advected, and the Ekman bottom boundary layer physics plays a key role on the dynamics of these coastal currents, besides wind forcing and ambient currents. Bottom-advected coastal currents can also have an upstream penetration along the coast (opposite direction to propagation of coastal-trapped waves), potentially carrying a significant fraction of the freshwater (Matano and Palma 2010). For intermediate cases, when $A_s \approx A_b$, the coastal currents exhibit a mixture of both types of coastal current characteristics.

The velocity of the coastal current may be obtained by taking advantage of the fact that its cross-shelf balance is geostrophic, which in a reduced gravity model on an f plane, can be written as

$$fv = g'\frac{dh}{dx}, \tag{1}$$

where $g' = g(\rho_o - \rho_p)/\rho_o$ is the reduced gravity. Therefore, by knowing the front slope, the density differences between the ocean and the coastal current, and latitude, one can estimate the velocity of the coastal current from Eq. (1).

Coastal current dynamics described above can be highly impacted by wind forcing through Ekman dynamics (e.g., Münchow and Garvine 1993b; Fong et al. 1997; Whitney and Garvine 2005). Upwelling-favorable winds advect surface waters offshore through Ekman transport, increasing W_s, and a return-compensating flow is observed in the bottom, which decreases h_p, flattening the isopycnals. Downwelling-favorable winds act in the opposite sense, advecting surface waters inshore, decreasing W_s, while there is an increase in h_p, steepening the isopycnals (Lentz and Largier 2006).

These modifications of the coastal current geometry by the wind have a direct effect on the geostrophic velocities and transport, through the modification of the thermal wind shear, as can be seen from Eq. (1). This way, downwelling-favorable winds can significantly increase the along-shelf transport and velocities, while upwelling-favorable winds decrease the along-shelf transport, and if persist long enough, the current may be detached from the coast and even reversed. We will use the extensive glider dataset to test the various theoretical and modeling results presented above. Last, in addition to wind forcing, other factors such as tides (Garvine 1999) and waves (Gerbi et al. 2013) have also shown to be important components that may affect mixing and modify the transport of coastal currents, but are not considered here.

2. Data and methodology

a. Observations

The Glider Research Group at OSU (http://gliderfs2.coas.oregonstate.edu/gliderweb/) has been surveying the Oregon coast since 2006, maintaining a nearly continuously operation along the NH-line (Fig. 1). The NH-line is located offshore of Newport, Oregon, along the latitude 44.65°N, and the glider operation surveyed approximately between 2 and 310 km offshore.

Underwater gliders are autonomous underwater vehicles (AUVs), driven by changes of buoyancy rather than using a propeller for propulsion; therefore, they are very energy efficient. Moving through the water column in a sawtooth pattern, they are controlled from land and provide real-time data through the use of satellite telephone communication. Two different types of autonomous underwater vehicles have been used on the NH-line surveys, the Slocum gliders from Teledyne Webb Research (Schofield et al. 2007) and the Seagliders from the University of Washington Fabrication Center (Eriksen et al. 2001).

The Slocum gliders were deployed near the coast (2 km) using the OSU research vessel (R/V) *Elakha*, between the 25- and 30-m isobaths. The Slocum gliders sampled up to 80 km offshore, reaching a maximum depth of 200 m, and take between 3 and 5 days to complete the line. In intervals between 3 and 6 h, gliders reach the surface and communicate to the Glider Research Group base station, transferring decimated data and receiving route adjustments, based on either scientific or operational needs. Batteries lasted for nearly 3 weeks after which gliders were recovered, and a second glider with fresh batteries was immediately deployed. The gliders' onboard instruments consisted of a temperature, conductivity, and pressure sensor (Sea-Bird Electronics, Inc., SBE-41CP); an altimeter to measure the height above the bottom; and a bio-optical sensor [WET Laboratories, Inc., Environmental Characterization Optics (ECO) Puck] to measure light backscatter (at 650 nm) and colored dissolved organic matter fluorescence (370-nm emission, 460-nm detection). Latitude and longitude were determined via GPS, and dive-averaged horizontal velocities were calculated from dead reckoning.

The Seagliders were deployed about 28 km from the coast, from the R/V *Elakha* near the 100-m isobath and

sampled up to 310 km offshore. The Seagliders reach a maximum depth of 1000 m, and take between 7 and 8 days to complete the line. After each dive, the Seaglider surfaces and communicates to the Glider Research Group base station and transfers data and any needed route adjustments. Batteries lasted for nearly 5 months, after which gliders were recovered for battery replacement and sensor calibration before they were redeployed. The Seagliders' onboard sensors were the same as those onboard the Slocums.

The data from the gliders used in this paper consist of temperature, conductivity, and pressure, collected at 0.5 Hz, and dive-averaged horizontal velocities calculated between surfacing intervals. Temperature and conductivity data from Slocum gliders were cleaned by removing spikes, and then salinity was estimated from conductivity and temperature by applying a thermal lag correction to the conductivity data following Garau et al. (2011). Density was then calculated from temperature, salinity, and pressure, using the 1980 equation of state (EOS-80).

Data from both Slocums and Seagliders are included in section 3a, since during the upwelling season the influence of the Columbia River extends farther offshore of the shelf break, and the Slocum trajectories did not capture the full extent of the Columbia River plume. The rest of the paper uses data solely from Slocums, since the focus is on the fronts trapped to the coast, and their cross-shelf extents were found to be typically less than the offshore distance covered by the Slocums.

All the fields were linearly interpolated to a two-dimensional grid, longitude versus depth, with a vertical resolution of 2 m and a horizontal resolution varying between 0.4 and 1 km for the Slocums, and 1–7 km for the Seagliders, to be consistent with the glider surfacing distances increasing in the offshore direction.

Glider data used in the buoyant fronts analysis for the downwelling season defined following Pierce et al. (2006) (available online at http://damp.coas.oregonstate.edu/windstress) were reinterpolated using Barnes objective analysis (Barnes 1994). The Barnes objective analysis used a decorrelation scale of 5 m in the vertical and 5 km in the horizontal, the latter approximately the local internal Rossby radius of deformation. The Barnes objective analysis helps filter out the higher-frequency, nongeostrophic part of the signal and allows for the calculation of less noisy density gradients. The 5-km spatial scale is equivalent to a filter with a time scale between 5.6 and 9.4 h.

Wind velocity data were obtained from the coastal station NWPO3 (44.6°N, 124°W) at Newport, from the National Data Buoy Center [National Oceanic and Atmospheric Administration (NOAA)], and wind stress was computed based on Large and Pond (1981). Current measurements were obtained from a downward-looking acoustic Doppler current profiler (ADCP) attached to the surface buoy NH10 (44.6°N, 124.3°W), with periods analyzed between 9 February 2007 and 10 March 2007, 11 October 2009 and 23 February 2010, and 30 November 2010 and 20 December 2010, a total of 166 days. Current velocities and wind stress were low pass filtered (40-h cutoff) to remove tidal and diurnal frequency signals and then were daily averaged. Gaps in ADCP data near the surface and bottom were filled using a slab model, since along-shelf current shear is very weak during these seasons. Geographical locations of coastal station NWPO3 and the surface buoy NH10 are shown in Fig. 1. NH10 is offshore of the front the majority of the time, since it is located 20-km offshore and is thus a reasonable location at which to estimate wind-driven current response.

b. *Estimating freshwater content and frontal characteristics*

The freshwater content of the water column was calculated using

$$F_s(x) = \int_{-D(x)}^{0} \frac{s_0 - s(x,z)}{s_0}\, dz, \qquad (2)$$

where $s(x, z)$ is the measured salinity, s_0 is the reference salinity, the quantity $[s_0 - s(x, z)]/s_0$ is the freshwater anomaly, and D is the depth at which s_0 occurs. The quantity F_s represents how many meters within the water column are due to purely freshwater, as if the freshwater could be unmixed from the oceanic saltwater. The value chosen for the reference salinity was $s_0 = 32.5$, as adopted by Barnes et al. (1972), as a typical value for the Columbia River–influenced water.

Far away from the source region, the dynamics of buoyant fronts trapped to the coast are tightly related to its geometry, which can be described by a small set of parameters (Fig. 2), such as W_p, W_s, W_b, ρ_o, ρ_p, h_p, and $h(x)$, as discussed before. To estimate these basic parameters describing the plume geometry from observations, only the glider transects in which the maximum absolute cross-shelf density gradient observed at the surface was at least 0.05 kg m^{-3} km^{-1} and the minimum density (and salinity) occurred inshore of this maximum absolute gradient were selected for the analysis. The latter choice ensures that the buoyant plume is adjacent to the coast.

The isopycnal that traced the offshore limit of the coastal current ρ_o was determined by finding the density value located at a specific fraction of the maximum surface density gradient in the offshore direction: $\partial\rho/\partial x| = (1/\gamma)(\partial\rho/\partial x)_{\max}$,

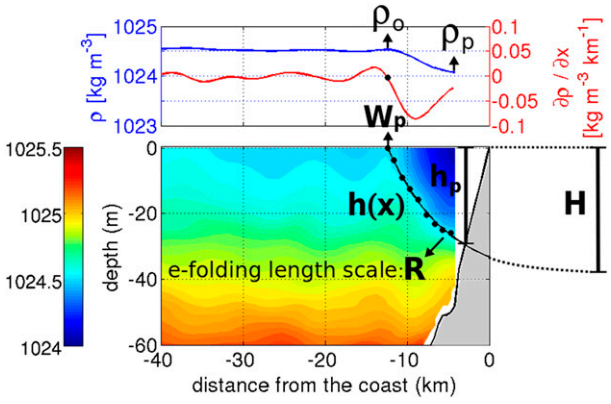

FIG. 3. Schematic showing one example of fitting Eq. (3) to a buoyant front, measured between 10 and 14 Jan 2011. (top) Cross-shelf surface density ρ (blue) and density gradients $\partial\rho/\partial x$ (red) and the dot shows where the front is located at the surface, according to $(1/\gamma)(\partial\rho/\partial x)_{\max}$, where $\gamma = 10$. (bottom) Colored contours of density field; dots show the discrete positions of the front and the fit to the front (solid line). The main parameters used from the fit are also indicated: W_p, h_p, H, R, ρ_o, and ρ_p.

where we have chosen $\gamma = 10$ (Fig. 3). The choice of $\gamma = 10$ was very robust, in the sense that when reducing it to half, $\gamma = 5$, none of the derived parameters varied significantly, with maximum variation observed for the baroclinic transport of only about 5% reduction. For the choices below $\gamma = 5$, a rapid decrease was observed in all the parameters, reaching minimum values when $\gamma = 1$, with reductions of 60% for baroclinic transports, 35% for h_p, 20% for W_s, and 5% for g'. Sensitivity tests were also made to the choice of decorrelation scales of the Barnes objective analysis. By doubling the decorrelation scales, from 5 to 10 m in the vertical and from 5 to 10 km in the horizontal, the baroclinic transports increased by only 2%, h_p increased 4%, and W_s increased 20%, while g' decreased by 5%.

Transects in which the frontal isopycnal also intersected the surface inshore of the maximum gradient were not considered "trapped" to the coast and were therefore excluded from the analysis. A total of 103 glider transects during fall–winter seasons [defined according to Pierce et al. (2006)] were examined, and 36 were removed from the analysis due to isopycnals outcropping inshore of the maximum gradient, with 22 of those found within a month after the fall transition. Often, the place where the front intersected the bottom, a key parameter in understanding coastal current dynamics, was located inshore of the glider data. To overcome this problem a model was fitted to the data, allowing extrapolation of the front inshore of the data domain. A total of 67 transects were analyzed, and the buoyant fronts were described by fitting an exponential function of the form

$$h(x) = H\{1 - e^{-[(x+W_p)/R]}\} \tag{3}$$

to the isopycnal positions, where $z = -h(x)$ is the vertical position of the front as a function of distance from the coast, $x = -W_p$ is the position of the front at the surface, R is the exponential function decay rate, and $z = -H$ is the layer depth far away from the front ($x \to \infty$). The choice of this function is primarily motivated by having the same form as the solution for the Rossby adjustment problem using a reduced gravity model (Cushman-Roisin and Beckers 2011), which describes the final shape of a front in an unbounded, unforced system adjusted under rotation. In that case, R would represent the Rossby radius of deformation defined as $R = \sqrt{g'H}/f$, where $g' = g(\rho_o - \rho_p)/\rho_o$ is the reduced gravity, and f is the Coriolis parameter. Secondarily, this model is a natural next step in complexity from the traditional straight interface Margules front model (Margules 1906), adopted in several studies to represent buoyant fronts and plumes (e.g., Garvine 1999; Fong and Geyer 2002; Lentz and Helfrich 2002). The exponential model proposed here would not be expected to work for nearly vertical fronts, such as the Chesapeake Bay plume under strong downwelling winds (Lentz and Largier 2006); however, those are rarely observed off the Oregon coast, possibly due to the large shelf steepness, compared to the east coast of the United States.

The function Eq. (3) was fitted by a numerical algorithm that minimized the root-mean-square error (RMSE) between the function and data, and three parameters were determined: W_p, R, and H. Since the fit of Eq. (3) is nonlinear, and there is no analytical solution for uncertainties of the fit parameters, a sensitivity test was conducted by varying each of the three parameters, W_p, R, and H, by $\pm 10\%$.

c. Frontal characteristics and wind stress

As shown in previous works (e.g., Lentz and Largier 2006; Moffat and Lentz 2012), the alongshore component of the wind stress can tilt the isopycnals through basic Ekman dynamics by pushing the front against the coast in downwelling-favorable winds or pulling the front away from the coast in upwelling-favorable winds. To investigate the response of the fronts to the wind forcing, a one-sided exponential decay filter was applied to wind stress:

$$W_k(t) = \frac{\int_{-\infty}^{t} \tau_o^y(t') e^{-[(t-t')/k]}\, dt'}{\int_{-\infty}^{t} e^{-[(t-t')/k]}\, dt'}, \tag{4}$$

where τ_o^y is the along-shelf wind stress, and k is the number of days (Austin and Barth 2002b). The time

scale for the plume response to the wind forcing was determined by finding the filter width k that maximizes the correlations between the filtered wind stress and the front tilt (h_p/W_s), which was found to be $k = 4$ days. The filtered wind stress was then compared to several plume characteristics and used on the transport calculations. In this paper, wind stress will always be referring to the filtered wind stress W_k, unless stated otherwise.

d. Velocity calculations

The geostrophic, or buoyancy-driven, velocities of the coastal currents v_b can be calculated analytically using $h(x)$ from Eq. (3), and the geostrophic balance in a reduced gravity model on an f plane [Eq. (1)], and can be written as

$$v_b(x) = \frac{g'H}{fR} e^{-[(x+W_p)/R]}. \tag{5}$$

The wind-driven velocity v_w was estimated following Lentz and Largier (2006), by assuming a frictional balance (balance between wind stress and bottom stress), and can be written as

$$v_w = \frac{\tau_o^y}{\rho_o r}, \tag{6}$$

where τ_o^y is the along-shelf wind stress, and r is a linear drag coefficient.

A third important contribution to the velocities during fall/wintertime off the Oregon coast is the seasonal large-scale Davidson Current. To estimate both the linear drag coefficient r and the Davidson Current v_D a linear regression analysis was made between depth- and daily-averaged currents from the NH10 mooring (v_{NH10}) during fall and winter and daily-averaged wind stress (τ_o^y/ρ_o) obtained from the coastal meteorological station NWPO3:

$$v_{\mathrm{NH10}} = \frac{\tau_o^y}{\rho_o r} + v_D, \tag{7}$$

where r is the inverse of the slope (1/slope), and v_D is the intercept. Correlation between wind stress and depth-averaged currents is significant, 0.62 (with 95% confidence limit of 0.19), which supports the assumption of a frictional balance. Values obtained from the regression analysis were $v_D = 0.026\,\mathrm{m\,s^{-1}}$ with upper and lower 95% confidence interval limits of $v_D = 0.045\,\mathrm{m\,s^{-1}}$ and $v_D = 0.007\,\mathrm{m\,s^{-1}}$, respectively, and $r = 9.7 \times 10^{-4}\,\mathrm{m\,s^{-1}}$ with upper and lower 95% confidence interval limits of $r = 12 \times 10^{-4}\,\mathrm{m\,s^{-1}}$ and $r = 8.1 \times 10^{-4}\,\mathrm{m\,s^{-1}}$, respectively. Lentz and Winant (1986) estimated linear drag coefficients at the southern California shelf and found values of $r = 4 \times 10^{-4}\,\mathrm{m\,s^{-1}}$ and $r = 5 \times 10^{-4}\,\mathrm{m\,s^{-1}}$ over the 60- and 30-m isobath, respectively, for fall and winter. The authors found that values over the 15-m isobath were roughly twice as large, $r = 9 \times 10^{-4}\,\mathrm{m\,s^{-1}}$ for fall and $r = 12 \times 10^{-4}\,\mathrm{m\,s^{-1}}$ for winter, within the same range of values obtained here. They attributed the increase of the linear drag coefficients over the shallower depths to the action of surface gravity waves (e.g., Grant and Madsen 1979). The action of waves could possibly explain the relatively high coefficients found off Newport, since waves during the winter are significantly higher than southern California (e.g., Allan and Komar 2006).

Finally, the total velocity $v(x)$ of the coastal current was calculated by assuming that the buoyancy-, wind-, and Davidson-driven velocities can be linearly added:

$$\begin{aligned} v(x) &= v_b + v_w + v_D \\ &= \underbrace{\frac{g'H}{fR} e^{-[(x+W_p)/R]}}_{\text{buoyancy–driven}} + \underbrace{\frac{\tau_o^y}{\rho_o r}}_{\text{wind–driven}} + \underbrace{v_D}_{\text{Davidson Current}}. \end{aligned} \tag{8}$$

Notice that this model assumes spatial homogeneity of the wind-driven v_w and Davidson current v_D flows, while the buoyancy-driven v_b component varies in the cross-shelf direction.

e. Transport calculations

The volume transport was estimated by simply integrating Eq. (8) over the plume area (derivation shown in the appendices), which leads to

$$\begin{aligned} Q &= Q_b + Q_w + Q_D \\ &= \frac{g'H^2}{2f}\left(1 + e^{-2W_s/R} - 2e^{-W_s/R}\right) \\ &\quad + \frac{\tau_o^y}{\rho_o r}\left[H(W_s + Re^{-W_s/R} - R) + \frac{W_b h_p}{2}\right] \\ &\quad + v_D\left[H(W_s + Re^{-W_s/R} - R) + \frac{W_b h_p}{2}\right]. \end{aligned} \tag{9}$$

The freshwater transport was calculated by integrating the velocities multiplied by the freshwater anomaly $\{[s_0 - s(x, z)]/s_0\}$:

$$Q_{\mathrm{fresh}} = \int\int v(x)\frac{s_0 - s(x,z)}{s_0}\,dx\,dz. \tag{10}$$

In the region inshore of the glider transect, where there is no data, the gap in salinity was filled up by reproducing the measured value closest to the coast for

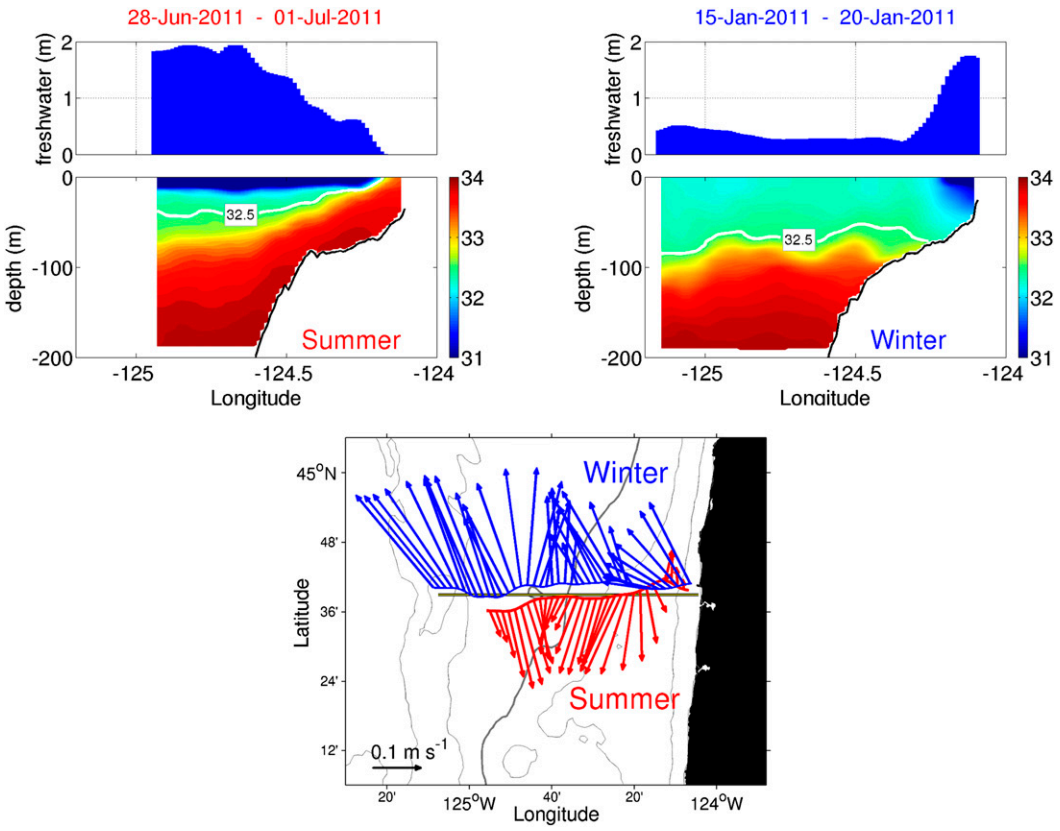

FIG. 4. Typical examples of freshwater content (m) calculated from Eq. (2) using (top) $s_0 = 32.5$ and (bottom) salinity fields observed off NH-line during (left) upwelling and (right) downwelling seasons. Glider tracks and depth-averaged velocities are shown in the lowest panel.

each depth. The extrapolation in salinity helped to complete the glider transects all the way to the coastline, allowing us to estimate the freshwater transport. To estimate the freshwater transport, the velocity within the coastal current $v(x)$ was obtained from Eq. (8), then multiplied by the freshwater anomaly field and integrated numerically.

3. Results

a. *Seasonal variability in freshwater off the coast of Oregon*

Typical glider cross-shelf sections showing major differences in freshwater regimes and oceanographic conditions between summer and winter are illustrated in Fig. 4. Freshwater content calculated from Eq. (2) using a reference salinity of $s_0 = 32.5$ reveals that during summer freshwater is absent inshore of the 70-m isobath and increases in the offshore direction, reaching a maximum value of nearly 2-m offshore of the 200-m isobath, where it maintains its value until the end of the glider transect. The 32.5 isohaline is marked on the salinity transect, which shows that its position in the water column lies between 30 and 50 m deep and decreases toward the coast, until it finally outcrops near the 70-m isobath. The isohalines, as well as the isotherms and isopycnals (not shown), tilting upward toward the coast are typical of summertime off the Oregon coast, as a result of the equatorward, upwelling-favorable winds, which are also responsible for the southward advection of these freshwaters from the Columbia River. The glider measures dive-averaged currents to the south.

A very different picture is observed during the wintertime. The freshwater content is at maximum near the coast, roughly 1.8 m, slightly smaller than the summer peak value, and decays rapidly in the offshore direction, where it keeps a nearly constant value of around 0.3 m offshore of the 80-m isobath until the end of the glider transect. A buoyant plume is found trapped to the coast, with the foot of the front located inshore of the 50-m isobath. The position of the 32.5 isohaline is deeper than during the summertime, lying between 70 and 80 m deep. Above the 32.5 isohaline and offshore of the coastal current, the water column is well mixed both horizontally and vertically due to the strong winds during this season. Below this well-mixed region, the isohalines, as well as

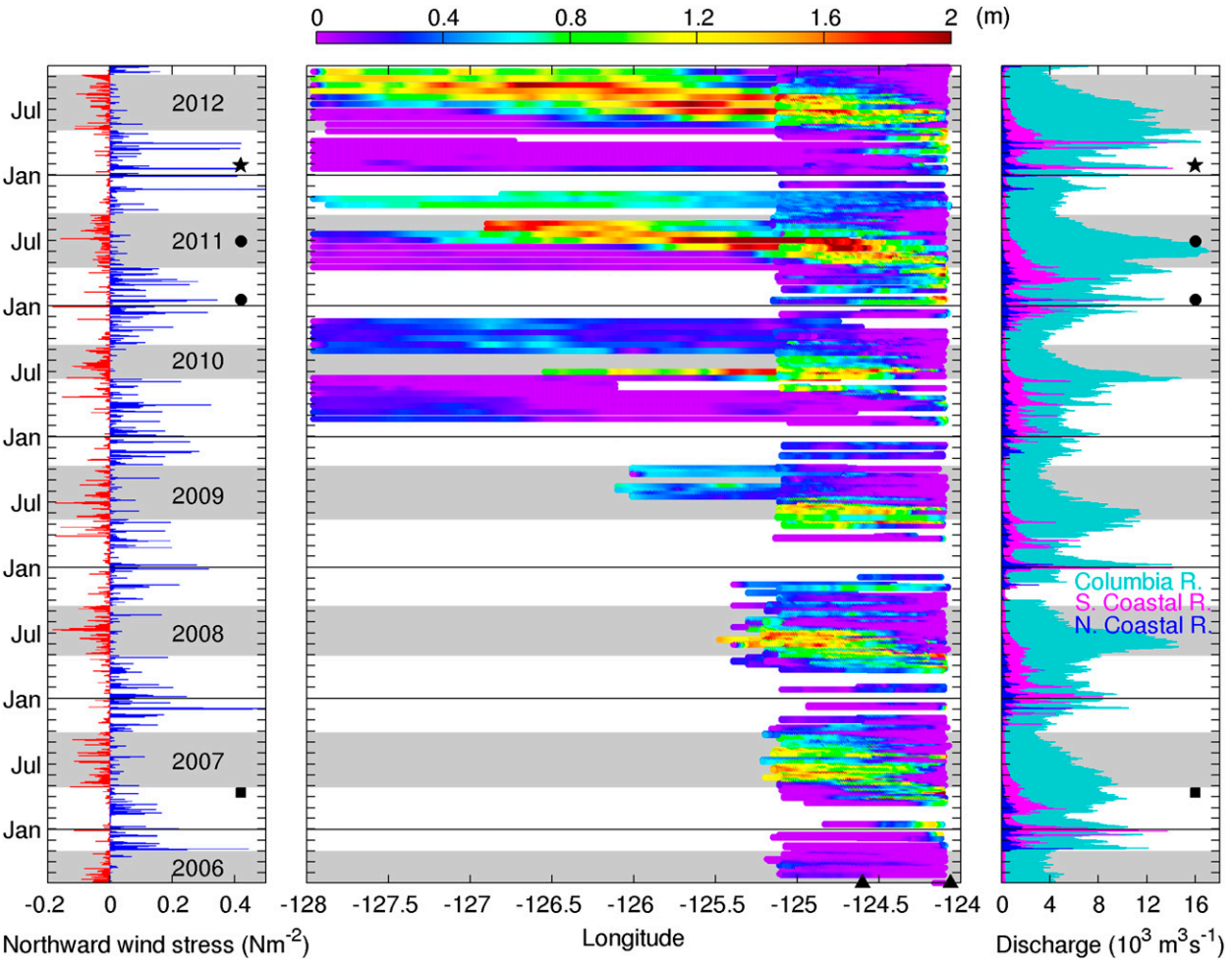

FIG. 5. (center) Time and space variations of freshwater content (m) along the NH-Line using $s_0 = 32.5$. The position of the coast and the 200-m isobaths are indicated by triangles. (right) The discharge from the Columbia River and the sum of discharges from gauged rivers south of the NH-line (southern coastal rivers), Yaquina, Alsea, Siuslaw, Umpqua, Coquille, Rogue, and Chetco Rivers in southern and central Oregon and Smith and Klamath Rivers in northern California, as well as north of the NH-line (northern coastal rivers), Siletz, Nestucca, Tillamook, and Nehalem Rivers. The geographical locations of the rivers along the coast are indicated in Fig. 1. (left) The daily averaged (nonfiltered) northward wind stress. The gray stripes indicate upwelling season according to Pierce et al. (2006) (available at http://damp.coas.oregonstate.edu/windstress). River discharge data obtained from the U.S. Geological Survey (USGS) and from the Oregon Water Resources Department (OWRD). In the right and left panels, the star indicates the time for the satellite image shown in Fig. 1, dots indicate the time of the transects shown in Figs. 3 and 4, and the square indicates the time of the transects shown in Figs. 9 and 14.

the isotherms and isopycnals (not shown), are tilted downward toward the coast, which is typical of wintertime off the Oregon coast, as a result of the poleward, downwelling-favorable winds. The glider measures dive-averaged currents to the north, nearly 10%–20% stronger than what was observed during summertime.

To understand the differences in the scenarios described above as well as the details of the seasonal evolution of freshwater content off the Oregon coast, 499 Slocum transects between 2006 and 2012 and 71 Seaglider transects between 2009 and 2012 are analyzed. Freshwater content using a reference salinity of 32.5 is shown as a Hovmöller diagram in Fig. 5. Also plotted are the wind stress time series and both the Columbia River discharge as well as the sum of the gauged coastal rivers between northern California and the NH-line (shown in Fig. 1). The upwelling seasons are determined following Pierce et al. (2006) (available at http://damp.coas.oregonstate.edu/windstress) and indicated by gray stripes.

During the upwelling season, the freshwater is found mainly on the mid- and outer shelf, advected southward from the Columbia River and held offshore by upwelling-favorable winds. The full cross-shore extent of the

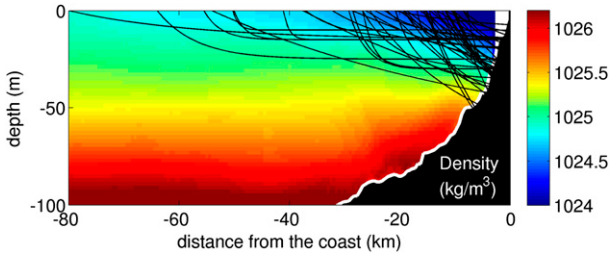

FIG. 6. Average density field overlaid with fitted fronts. In this calculation, only fronts that were located within 20 km north and south from the NH-line were chosen (79%).

freshwater is only captured when using both the Slocums and Seagliders, particularly visible for 2011 and 2012, when there is a higher spatial and time coverage available. Discharge peaks from the Columbia River are in phase with the peaks of freshwater content. A continuous offshore propagation of both the inshore and offshore regions of the freshwater (Columbia River plume) occurs throughout the seasons due to a cumulative effect of upwelling-favorable winds. Columbia River discharge during 2011 and 2012 is higher than normal conditions, associated with a strong La Niña event, and as a result higher freshwater content is observed off the central Oregon coast, compared to the previous years (Mazzini et al. 2011). During downwelling season, the freshwater is found mostly adjacent to the coast and confined in a much smaller cross-shore region. The peaks in freshwater content are in phase with peaks of coastal (non-Columbia River) river discharge, which suggests the freshwater is being advected toward the north.

b. Front characteristics

The results of the fitted fronts, $h(x)$ computed from Eq. (3), are shown in Fig. 6, overlaying the average density field computed using only fronts that were located 20 km north and south from the NH-line, 79% of the total. A clear density gradient is observed, where inshore waters are less dense (below 1024 kg m^{-3}) than offshore waters (approximately 1025 kg m^{-3}) in the upper ocean.

Probability density functions of the main parameters that characterize the fitted fronts, such as W_p, W_s, W_b, h_p, ρ_o, ρ_p, $\Delta\rho$, H, and R, are shown in Fig. 7. The coastal currents total width W_p encompasses a wide range of values, from 5 to over 70 km; however, the majority of observations (over 80%) lie between 10 and 30 km. The part of the front that is not in direct contact with the bottom W_s ranges from 5 to over 70 km, with over 50% of observations equal to or larger than 15 km. The part of the front that is in direct contact with the bottom W_b is much smaller than W_s, roughly one order of magnitude, ranging from 0.5 to 7 km. The thickness of the coastal currents h_p, which is directly related to W_b (for a constant slope of the ocean bathymetry), ranges from 5 to 70 m thick, with approximate 70% of observations between 15 and 40 m thick.

The ocean density, represented by ρ_o, varies between 1023 and 1025.5 kg m^{-3}, with over 50% of the observations falling in the 1025 kg m^{-3} class. A broader distribution is seen in the coastal current density ρ_p, ranging from 1021.5 to 1025 kg m^{-3}, with over 95% of observations falling between 1023 and 1023.5 kg m^{-3}. The typical density difference between the ocean and coastal current $\Delta\rho = \rho_o - \rho_p$ is between 1 and 2 kg m^{-3} for over 45% of the observations and between 0.5 and 1 kg m^{-3} for nearly 30% of observations.

For the exponential fits [Eq. (3)], nearly 50% of the H values fall between 20 and 40 m deep and 30% between 180 and 200 m deep, resembling a bimodal probability density function. Note that in the fits, H was limited to a maximum value of 200 m because it is not possible to cover the full range of possible values for H, since if the front becomes very steep (e.g., because of downwelling-favorable winds), $H \rightarrow \infty$. Over 45% of R values are observed at the 0–10-km class, and nearly 75% fall between 10 and 30 km.

c. Front response to wind forcing

The geographical location of the fronts (W_p and h_p) are shown in Fig. 8, with vectors representing the nonfiltered daily averaged wind stress (left), as well the filtered version (right), using Eq. (4). The location where the front contacts the bottom (the "foot") h_p is located inshore of the 50-m isobath for the vast majority of the cases. Also, for only a few cases did the glider data sample the location of h_p, and therefore fitting Eq. (3) was a necessary tool for determining the location of h_p. The cross-shelf location of W_p is much more variable than h_p and covers a wide range of values, anywhere from 7 to over 70 km offshore. Notice that the data are biased toward the north of NH-line, since the gliders often drifted northward due to the strong currents occurring during fall/winter, as can be seen by a few examples of the glider tracks also plotted in Fig. 8.

The nonfiltered wind stress vectors show that the fronts were measured at very different wind conditions, covering almost all directions, although the southward (upwelling favorable) wind stress vectors are in general much smaller than the northward (downwelling favorable) ones, consistent with wind regime off the Oregon coast during fall/winter. A much cleaner and organized picture is observed after filtering the wind stress data, and it can be seen that for the fronts located farther offshore, the wind stress was very weak or upwelling favorable, while the vectors increase and become downwelling

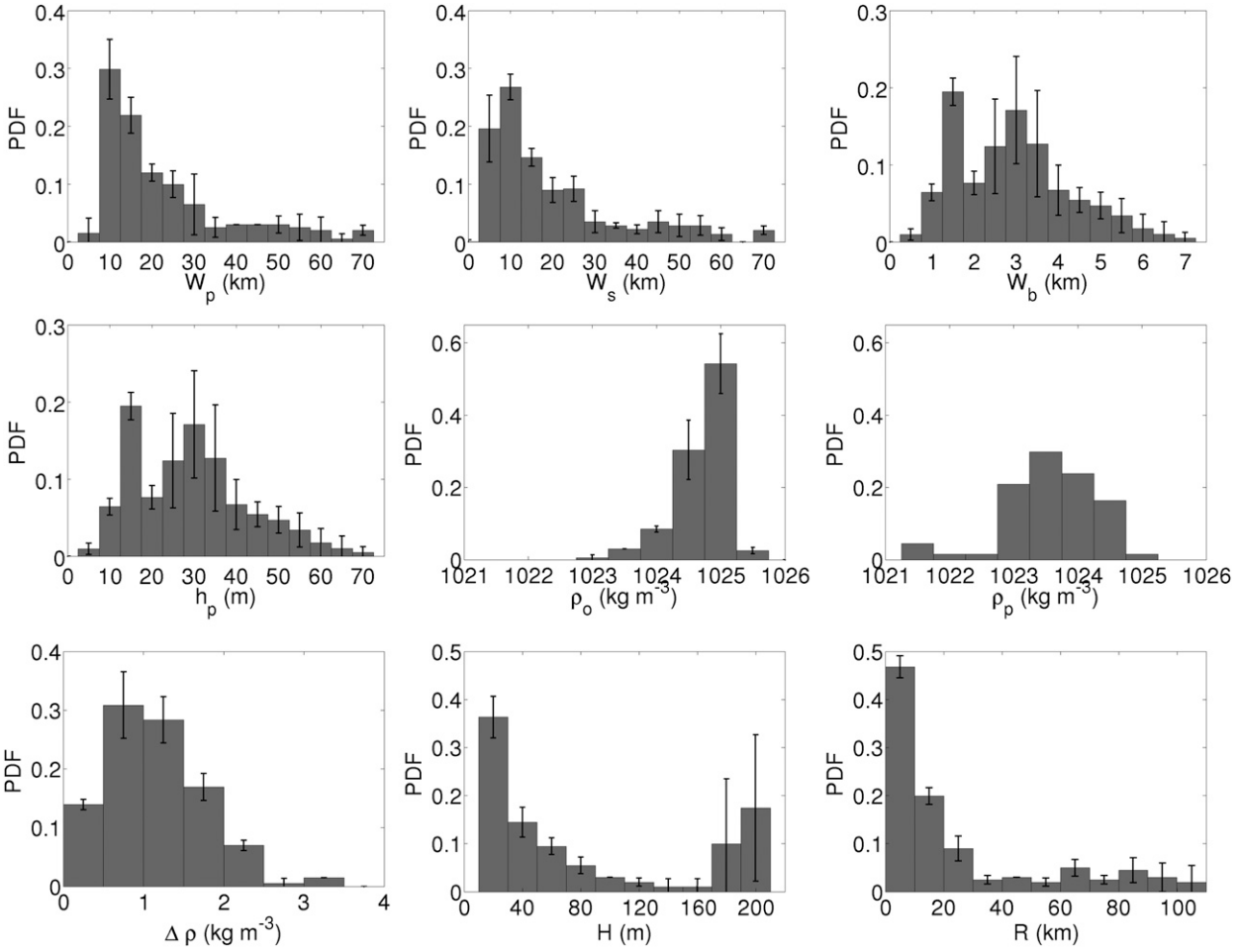

FIG. 7. Probability density functions of main plume parameters from observations: W_p, W_s, W_b, h_p, ρ_o, ρ_p, $\Delta\rho$, H, and R. Error bars are standard deviations for each class, obtained from the sensitivity analysis of each fit parameter (W_p, H, and R).

favorable rapidly as the fronts get closer to the coast. This behavior is consistent with Ekman dynamics as shown in previous works, where upwelling-favorable winds advect the surface fronts offshore, thinning out the plume, and downwelling-favorable winds advect the surface fronts toward the coast (Fong and Geyer 2001; Lentz and Largier 2006; Moffat and Lentz 2012).

Another potential example of the effect of Ekman dynamics influencing the plume characteristics and geometry can be seen in the sequence shown in Fig. 9. The front is initially measured after a period of persistent downwelling-favorable winds, with a magnitude of 0.02 N m^{-2} on the day W_p was measured. The front position W_p was located just offshore of 20 km from the coast, and h_p was slightly over 34 m deep. A reversal to weak upwelling-favorable winds takes place and lasts nearly 5 days, with an average magnitude of 0.003 N m^{-2}, before the front is measured again. A drastic change in the plume geometry is observed: W_p expands to nearly 55 km offshore, and h_p thins to nearly 25 m deep. The upwelling-favorable winds then cease and reverse again to downwelling favorable, and 2 days after this reversal, the front is measured again under a wind stress of 0.003 N m^{-2}. Position W_p is found nearly 19 km from the coast, just slightly inshore of its initial position, and h_p thickens out to 32 m, 2 m thinner than its initial thickness. The plume seems to be reset back to its approximate initial position, after only 2 days of downwelling-favorable wind stress; however, its area is smaller, and the front has a different e-folding length scale R.

Characteristics of the plume geometry such as W_p, h_p, W_s, W_b, the ratio W_s/W_b, the tilt of the front (h_p/W_s), as well as the RMSE of the fits as a function of wind stress are shown in Fig. 10. For very low wind stress, between $\pm$0.02 N m^{-2}, W_p covers a wide range of values, from typically 10 to 80 km, and as the wind stress increases, there is a rapid decrease in W_p that seems to be limited to no less than roughly 10 km. A similar pattern is

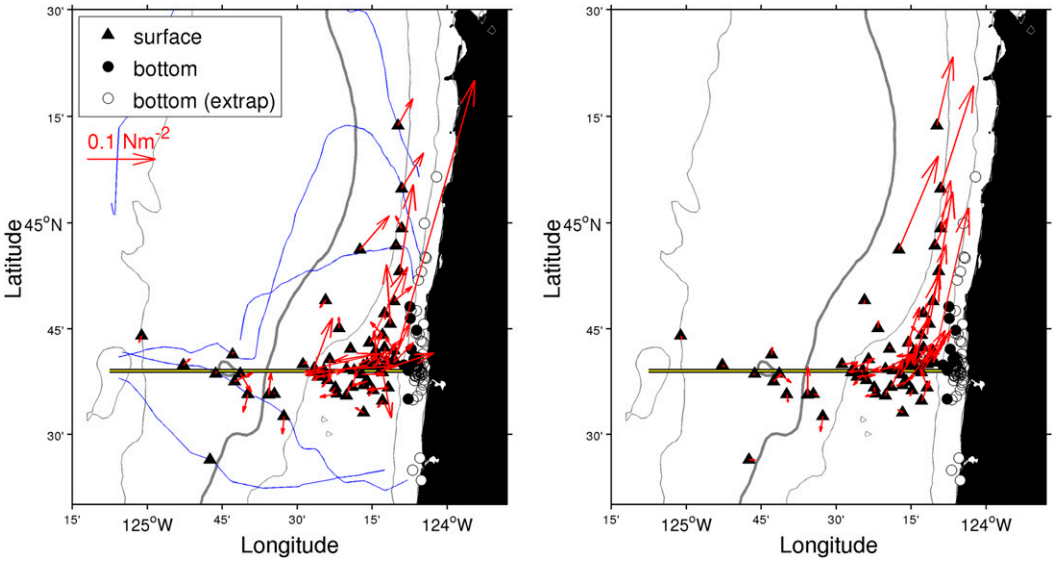

FIG. 8. Map showing surface and bottom front positions with (left) raw wind velocities vectors and (right) filtered velocity vectors. Triangles show where fronts intersect the surface, while circles show where fronts intersect the bottom. White circles represent instances when the glider data did not cover the area where the front intersected the bottom, so the position was extrapolated based on the fit of Eq. (3). On the left, only a few glider tracks are plotted in blue, for clarity. The NH-line is indicated by a straight line at 44°39′N, and isobaths of 50, 100, 200, and 1000 m are plotted. The thick gray line indicates the 200-m isobath.

observed for W_s, however, shifted between 1 and 7 km toward lower values, since it is defined as $W_s = W_p - W_b$, and it never reaches zero. A different pattern is observed in h_p, where the lowest values are found at low wind stress between slightly less than 10 up to 50 m, with most points falling around 30 m deep and increasing slowly as the wind stress increases, reaching up to over 60 m. The value of W_b has the same behavior as h_p since they are related by $W_b = h_p/\alpha$, where α is the bottom slope, taken to be 0.01.

The gray dashed lines in Fig. 10 represent what the positions of W_p and h_p (and W_b) would be if the front isopycnal became a straight vertical line, conserving the average plume area. This basically assumes that the plume has achieved its ''full downwelling'' response, that is, the front was tilted vertically by downwelling-favorable winds, reducing its offshore extent from W_p until it became vertical with the final offshore extent W_f and increasing its thickness h_p to a final thickness h_f. This was calculated using $h_f = \sqrt{\tan\alpha \overline{W_p}\,\overline{h_p}}$ and $W_f = h_f/\tan\alpha$, where $\alpha = 0.01$ is the bottom slope, chosen for typical Oregon inner shelf, and the overbars represent average values. The extent W_f is nearly 10 km and seems to well define a lower limit for W_p, where values of W_p are rarely smaller than W_f, with two clear exceptions at 0.15 and 0.23 N m^{-2}, which coincide with high values of RMSE. The value of h_f is close to 80 m, and values of h_p never cross h_f; in fact, its highest values are nearly 20 m shallower than h_f.

The ratio W_s/W_b indicates whether the fronts are surface trapped ($W_s \gg W_b$), bottom advected ($W_s \ll W_b$), or intermediate ($W_s \approx W_b$). Figure 10 shows that for very low wind stress, between ± 0.02 N m^{-2}, W_s varies from 2 to nearly 50 times larger than W_b. For downwelling-favorable wind stress values larger than 0.02 N m^{-2}, W_s vary from 5 times larger than W_b to $W_s \approx W_b$, with only one exception that $W_s < W_b$ for the highest value of wind registered within our data, of nearly 0.23 N m^{-2}. Over 95.5% of observations showed ratios W_s/W_b are above 1, and 82% are above 2, which demonstrates that for the vast majority of the cases, the coastal current is surface advected, while only 4% of observations had ratios W_s/W_b below 1 or bottom advected.

The front slope, defined as h_p/W_s, varies from nearly zero at wind stress with negative values close to 0 N m^{-2} and then increases as the wind stress increases, reaching values over 16×10^3. The RMSE, estimated based on the vertical position of the exponential fit model and the observed isopycnal that was used to trace the coastal current, varies from less than 1 to over 6 m, and has the greatest range around 0 N m^{-2} wind stress. The highest RMSE values are found for both wind stress close to 0 N m^{-2} and at high wind stress, exceeding 0.13 N m^{-2}. Moderate downwelling-favorable winds, around 0.1 N m^{-2}, give the lowest RMSE values, typically less than 2 m, and the best exponential fit within the limited number of data points available.

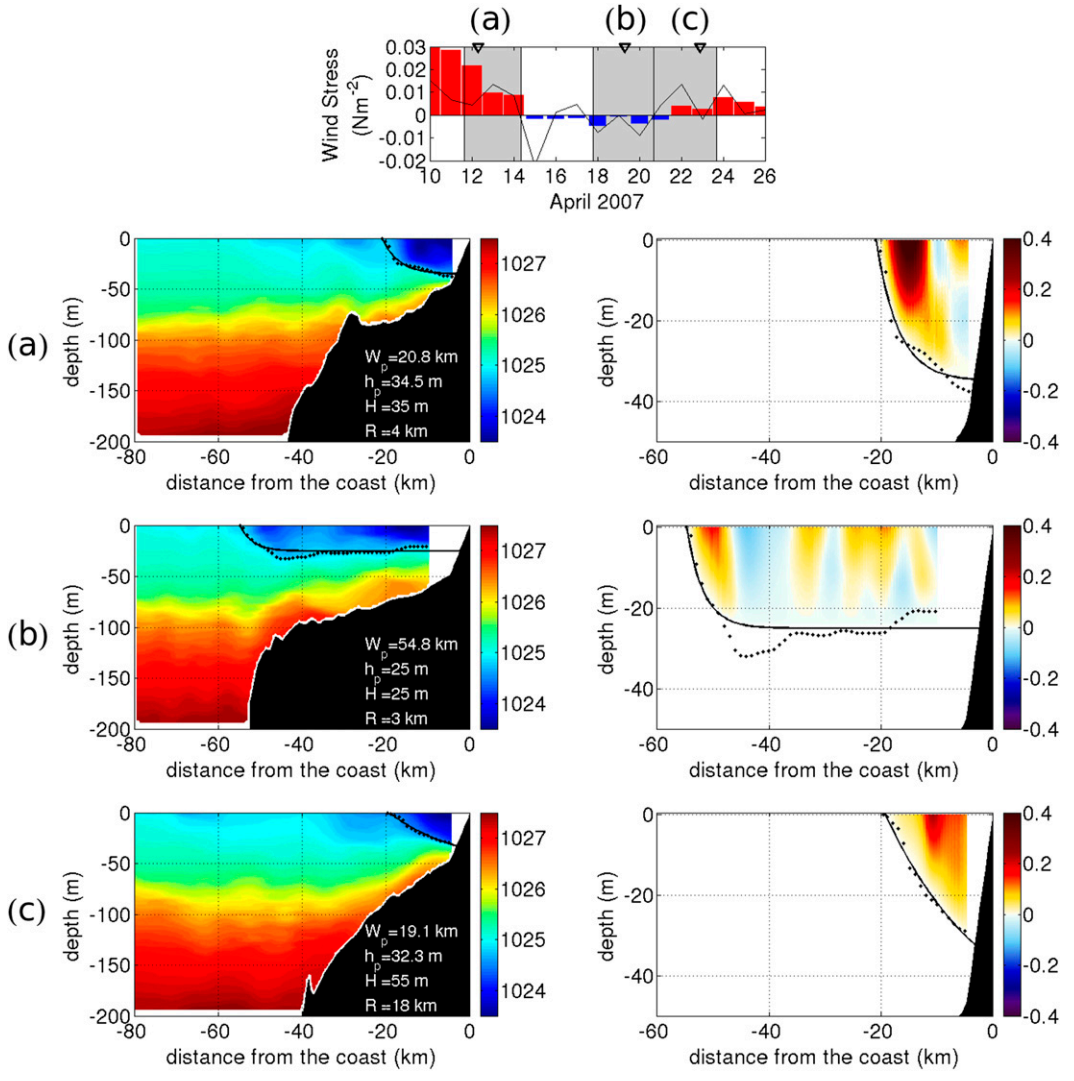

FIG. 9. (top) Filtered wind stress (bars) and nonfiltered daily averaged wind stress (black solid line). Below (left) density fields (kg m^{-3}) and (right) geostrophic velocities (m s^{-1}) showing a sequence of coastal currents under different wind stress conditions: (a) strong downwelling, (b) weak upwelling, and (c) moderate downwelling favorable. The geostrophic velocities were calculated based on the dynamic method using temperature and salinity fields from the glider data, zero referenced at the plume front. Dots represent discrete positions of the isopycnals overlaid with the fitted fronts (only half of the dots were plotted for clarity). The parameters W_p, h_p, H, and R are shown for each event. Shaded in gray in the top panel are the periods the glider took to complete each transect and upside down triangles are the times at which the fronts were measured. Note that the right column has zoomed into the coastal current to enhance the details of the geostrophic velocity field.

As previously discussed, the choice of fitting the exponential function [Eq. (3)] in order to represent the shape of the coastal current was motivated by having the same form as the solution for the Rossby adjustment problem in a reduced gravity model. The fitted parameter R would represent the Rossby radius of deformation, defined as $\sqrt{g'H}/f$, for this case. A comparison between R and $\sqrt{g'H}/f$, as a function of wind stress is presented in Fig. 11. The differences between R and $\sqrt{g'H}/f$ can reach over 90 km and are largest during weak wind events between $\pm 0.025\,\mathrm{N\,m^{-2}}$. For downwelling-favorable wind stress, above $0.025\,\mathrm{N\,m^{-2}}$, the differences between R and $\sqrt{g'H}/f$ tend to decrease, even though there is a clear presence of outliers. It is important to realize that the presence of the coast limits the extent of the front, when compared to an unbounded system (e.g., horizontally infinite ocean, no coast), as in the original Rossby adjustment problem. If we treat the front as unbounded, we assume that we only have information about a limited portion of the entire front, and small

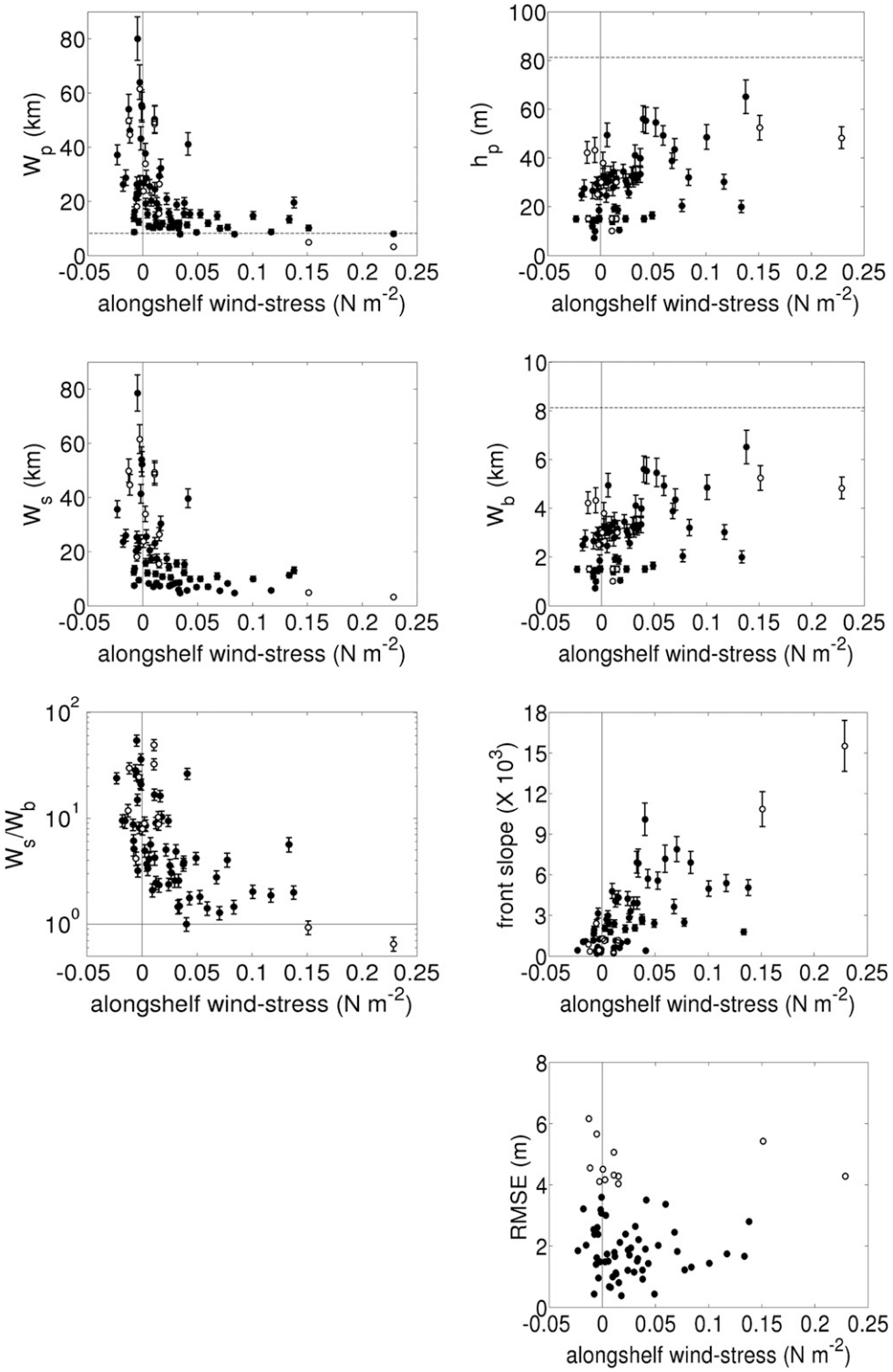

FIG. 10. Filtered wind stress vs absolute values of W_p, h_p, W_s, W_b, ratio W_s/W_b (ratio of 1 is indicated by a solid line), front slope or h_p/W_s, and the RMSE between isopycnal positions and the fitted function. Gray dashed lines show what W_p, W_b, and h_p would be if the front was completely vertical for an average plume area. Open circles indicate that RMSE was higher than the average RMSE plus one standard deviation. Error bars are standard deviations obtained from the sensitivity analysis of each fit parameter (W_p, H, and R).

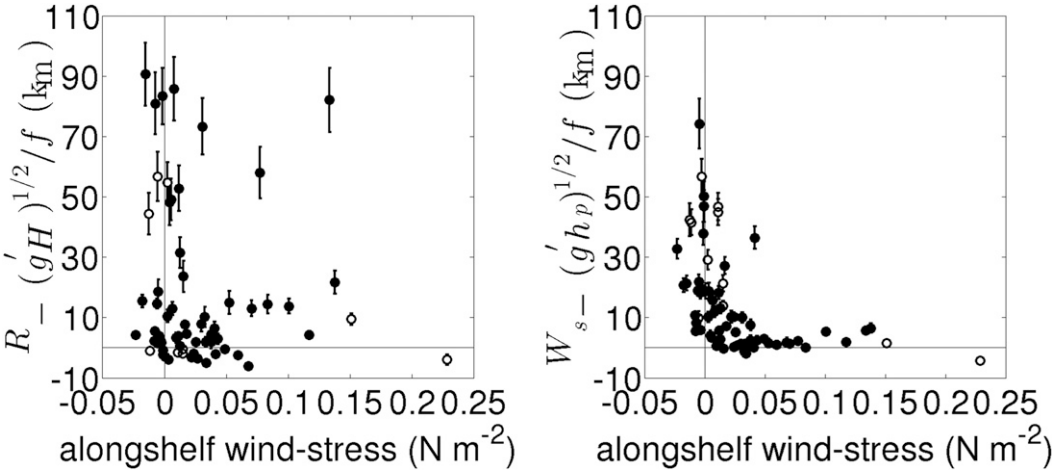

FIG. 11. Comparison of filtered wind stress vs different scalings for the Rossby radius of deformation (km): (left) $R-(g'H)^{1/2}/f$ and (right) $W_s-(g'h_p)^{1/2}/f$. Open circles indicate that RMSE was higher than the average RMSE plus one standard deviation. Error bars are standard deviations obtained from the sensitivity analysis of each fit parameter (W_p, H, and R).

perturbations could lead to large errors in R and H; hence, $\sqrt{g'H}/f$.

Previous studies of coastal currents with a sloping bottom have assumed that the geostrophic adjustment occurs offshore of the foot of the front h_p and that W_s scales as the Rossby radius of deformation, defined as $\sqrt{g'h_p}/f$ (e.g., Lentz and Helfrich 2002; Moffat and Lentz 2012). A comparison between W_s and $\sqrt{g'h_p}/f$, as a function of wind stress, is presented in Fig. 11. Differences between W_s and $\sqrt{g'h_p}/f$ tend to be much smaller than between R and $\sqrt{g'H}/f$, but still can reach over 70 km. A similar pattern is observed, where higher differences are observed for low wind stress, $\pm 0.025\,\mathrm{N\,m^{-2}}$, and the differences rapidly decrease as the wind becomes moderate downwelling favorable. For wind stress larger than $0.025\,\mathrm{N\,m^{-2}}$, $W_s \rightarrow \sqrt{g'h_p}/f$, and there are not as many contrasting outliers as observed in the case of $R-\sqrt{g'H}/f$. In this case, the parameters W_s and h_p are less sensitive than R and H; W_s is independent of the shape of the front, which could be curved or straight, and that would impact R, and even large variations of H would only lead to small variations in h_p.

d. *Along-shelf velocities and total and freshwater transport*

Total along-shelf velocities within the coastal currents, averaged in the A_s region, total transport estimates Q, calculated using Eq. (9), as well as the freshwater transports Q_{fresh}, computed from Eq. (10), are shown in Fig. 12. The fraction of each transport mechanism, buoyancy Q_b, wind Q_w, and Davidson driven Q_D, relative to the total transport and freshwater transport is also shown in Fig. 12.

For the total along-shelf velocities, over 30% of observations fall within the 0–0.1 $\mathrm{m\,s^{-1}}$ class, and about 15% fall within the 0.1–0.2 $\mathrm{m\,s^{-1}}$ class; then the distribution is nearly evenly distributed, and after reaching 0.6 $\mathrm{m\,s^{-1}}$, it tapers off linearly from 10% to nearly vanishing at approximately 1.1 $\mathrm{m\,s^{-1}}$.

Total transport values Q vary from less than 0.05 to over 0.5 Sverdrups (Sv; 1 Sv $\equiv 10^6\,\mathrm{m^3\,s^{-1}}$), with approximately 65% of transports lower than 0.1 Sv, nearly 21% between 0.1 and 0.2 Sv, and roughly 14% of values higher than 0.2 Sv. The higher end of these estimates is of the same order of magnitude as the coastal upwelling jet observed during summertime off the Oregon coast (Barth and Wheeler 2005). The coastal current is primarily buoyancy driven, accounting for over 61% (±22.6%) of the total transport, followed by the Davidson Current, which is responsible for nearly 26% (±18.6%), and finally, the wind forcing, which accounts for about 13% (±11.7%) of the total transport.

Freshwater transports Q_{fresh} vary from a few hundred to over 5000 cubic meters per second, the latter being the same order of magnitude as fall/winter peak discharges from the coastal rivers (Fig. 5). Nearly 41% of observations show discharges of less than $1\times10^3\,\mathrm{m^3\,s^{-1}}$, 30% between 1 and $2\times10^3\,\mathrm{m^3\,s^{-1}}$, and 29% above $2\times10^3\,\mathrm{m^3\,s^{-1}}$. The ratio of the mechanisms responsible for the freshwater transport, buoyancy, Davidson, and wind driven follow the same pattern as for the total transport, with relative contributions of 59% (±25.2%), 24% (±21.8%), and 17% (±14.6%), respectively.

A direct comparison between buoyancy-driven transports Q_b calculated from the exponential model [Eq. (A1)] versus transports calculated by the dynamic

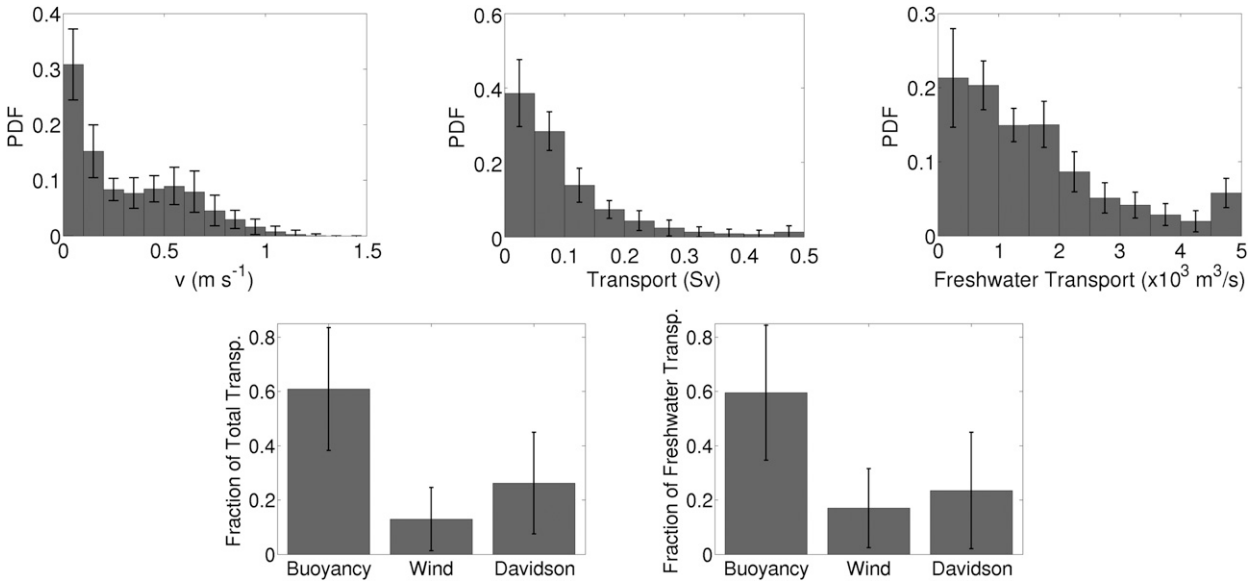

FIG. 12. Probability density functions of average velocities within the (top left) coastal current, (top middle) total transport, and (top right) freshwater transport. Ratios of buoyancy-, wind-, and Davidson-driven transports to the (bottom left) total transport and to the (bottom right) freshwater transport. Error bars are standard deviations for each class, obtained from the sensitivity analysis of each fit parameter (W_p, H, and R).

method using the temperature and salinity fields from the gliders are shown in Fig. 13. The level of no motion used in the dynamic method calculation was the front position obtained from the fit [Eq. (3)]. Transports from the exponential fit can get higher than 0.2 Sv, while smaller transports are observed from the dynamic method, reaching values slightly above 0.05 Sv. A linear regression between the transports, reveals a slope of 1:4 (±0.04, 95% confidence intervals), which demonstrates a consistent reduction in the transport estimated by the dynamic method, when compared to the two-layer exponential model. This reduction in the transport is consistent with the fact that the ocean is continuously stratified (laterally and vertically) (e.g., Pimenta et al. 2011; Moffat and Lentz 2012), and the two-layer assumption in the exponential fit model [Eq. (A1)] overestimates the transports.

An example of the geostrophic velocities computed from the dynamic method is show in Fig. 9, which demonstrates a higher spatial variability than a simple two-layer flow. The strongest northward velocities within the coastal current are in general located closer to the offshore boundary, where the fronts are steepest, and then decay toward the coast. Inshore of this steepest region, where the fronts tend to level, the lowest velocities are observed, and even small reversals toward the south, typically less than $0.05\,m\,s^{-1}$, are observed, especially under upwelling-favorable winds (Fig. 9b). The maximum observed velocities are also consistent with the wind forcing magnitudes; the highest velocities ($\sim 0.5\,m\,s^{-1}$) are associated with the strongest downwelling-favorable winds (Fig. 9a), followed by $0.24\,m\,s^{-1}$ velocities during weaker downwelling-favorable winds (Fig. 9c), and finally the smallest velocities, $0.17\,m\,s^{-1}$, during weak, upwelling-favorable winds (Fig. 9b).

4. Discussion

a. *Seasonal regimes of freshwater*

A seasonal cycle is remarkably clear in the freshwater content off the Oregon coast, and it is possible to separate two main distinct regimes: the spring/summer and the fall/winter (Fig. 5). The spring/summer season can be characterized by the presence of freshwater mainly from the mid- and outer shelf up to over a few hundred kilometers offshore, advected southward from the Columbia River and pushed offshore by upwelling-favorable winds (Barnes et al. 1972). A continuous offshore propagation of the Columbia River plume is apparent throughout the summer, as can be seen in Fig. 5, especially for the years of 2011 and 2012 when there were glider data available that could capture the entire cross-shore extension of the Columbia River plume. This is consistent with the cumulative effect of upwelling observed off the Oregon coast (Pierce et al. 2006). The change in the freshwater content from fall/winter to spring/summer seems to occur quite abruptly and fairly well predicted by the onset of the upwelling season according to the dates proposed by Pierce et al. (2006).

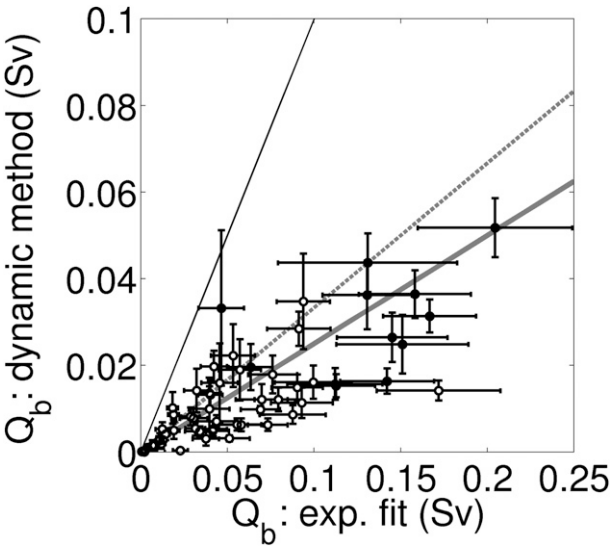

FIG. 13. Comparisons between the buoyancy-driven transports calculated using the exponential fit [Eq. (A1)] vs transports calculated from the dynamic method, using temperature and salinity fields from glider data and referenced to the front positions. Filled circles indicate transects in which the glider data covered the fronts all the way to the foot of the fronts h_p; 11 out of a total of 67. Black solid line indicates the 1:1 ratio, gray solid line was obtained from linear regression, and gray dashed line indicates a ratio of 1:3, which is the ratio of transports between a linearly stratified vs a two-layered Margules front. Error bars are standard deviations obtained from the sensitivity analysis of each fit parameter (W_p, H, and R).

During fall/winter, the freshwater is trapped to the coast and decays in the offshore direction. The change from spring/summer to fall/winter, however, seems to be a slower process in which the appearance of the freshwater is highly dependent on the onset in the coastal river discharges, driven by rainfall, which are not necessarily phase locked to the changes in wind regimes. A good example of this is apparent in fall/winter 2006 when the river discharges increase right after the end of upwelling season and freshwater readily appears versus 2010 when it takes up to 2 months before there is an increase in the coastal rivers' discharge and the subsequent appearance of freshwater off the NH-line (Fig. 5).

Variations in the freshwater content also coincide with variability of discharge peaks from the coastal rivers. The buoyancy forcing, Davidson Current, and wind stress, which is predominantly northward (downwelling favorable), act to advect freshwater toward the north (Fig. 12). Exceptions to that, when freshwater may be advected toward the south, for example, from the Columbia River, could possibly arise due to wind reversals. The wind forcing in this case would have to be strong enough in order to overcome both the buoyancy forcing and the Davidson Current. Observations of the Columbia River plume during the wintertime by Hickey et al. (1998) demonstrate that this is not the case, even in the presence of sustained upwelling-favorable winds. This is also supported by numerical simulations of an idealized Columbia River plume from Garcia Berdeal et al. (2002), which shows that the plume direction can only be reversed to the south in the presence of strong, persistent, upwelling-favorable winds, typically larger than 0.14 N m^{-2}, blowing over at least 2 days, events that are rarely observed during winter. Therefore, the low-salinity waters and the freshwater fronts observed off the coast of Newport, Oregon, mainly originated from coastal rivers (from the south), as previously hypothesized by Huyer (1977). Significant volume transports were observed from the coastal current off Newport, Oregon, of $O(0.1)$ Sv, comparable in magnitudes to the coastal upwelling jet observed during summertime (Barth and Wheeler 2005).

b. Coastal current dynamics

The choice of using of a two-layer model to characterize the coastal current overestimates the stratification, directly modifying the thermal wind shear and finally overestimating velocities and transports. Another model choice could be a straight, linearly stratified front with density varying linearly from the ocean density ρ_o to a minimum plume density ρ_p on the surface at the coast. For a similar geometry of a Margules front, but linearly stratified, the transport would be modified by a factor of 1/3, which in this case Eq. (B2) would simply become $Q_{b_{\text{stratified}}} = [(g' h_p^2)/(6f)]$ (Avicola and Huq 2003). Comparisons between transports from the exponential model and obtained from the dynamic method show a smaller ratio of 1/4 (Fig. 13). It is important to emphasize that most glider measurements do not have data all the way to the foot of the front h_p nor inshore of that, where there still may be significant lateral density gradients and therefore would have nonzero geostrophic velocities obtained from the dynamic method and possibly contribute to the transport. Those velocities inshore of h_p are not accounted for in the simple two-layer model.

If the effect of stratification were incorporated in our estimates by adopting a linearly stratified, straight front model instead of the two-layer exponential model, then the factor of 1/3 decrease in the buoyancy-driven transports would lead to a modification of the relative transports by each mechanism: buoyancy-driven transports would have a decrease of its relative contribution to 39.5% (±21.8%), becoming comparable to the Davidson current, with 40.1% (±21.3%), and the wind stress would still play a secondary role, but increased to 20.4% (±15.4%). It is important to emphasize that those estimates come from our simple model in which we assume that the mechanisms can be linearly added. By

using a primitive equation, three-dimensional numerical model, running both realistic and semi-idealized simulations, it would be possible to disentangle the relative importance of each forcing mechanism in driving the total transport, without relying on a priori assumptions.

A more detailed analysis on how the effect of stratification may impact the transport of coastal currents can be found in Pimenta et al. (2011), but in general, their results fall between the limits discussed above. This helps to understand how our estimates are impacted by stratification and at the same time give upper and lower bounds to our calculations. Despite the model choice, the order of magnitude of transports from the coastal currents would not change, and its role on the dynamics of the continental shelf off the Oregon coast during the fall/winter is vital.

The coastal current observed off the coast of Newport, Oregon, can be classified as surface trapped because the portion of the plume that is not in direct contact with the bottom W_s is generally one order of magnitude larger than the portion in direct contact with the bottom W_b. In addition, the total plume width W_p is rarely observed inshore of 10 km, and the thickness of the plume h_p is rarely smaller than 10 m. This implies that the coastal current structure and dynamics are highly susceptible to wind forcing and are not primarily controlled by the Ekman bottom boundary layer processes (Chapman and Lentz 1994).

The effect of the wind forcing on a buoyancy-driven coastal current is consistent with previous model results (Chao 1987) as well as observations (Lentz and Largier 2006). Upwelling-favorable (downwelling-favorable) winds drive offshore (onshore) Ekman transport associated with a compensating onshore (offshore) return flow, advecting the plume waters in the offshore (onshore) direction, and at the same time thinning (thickening) out the plume, which finally leads to a change in the isopycnals' slope (e.g., Whitney and Garvine 2005; Lentz and Largier 2006; Moffat and Lentz 2012). Nevertheless, the effect of three-dimensional variability, which may arise due to flow–topography interactions, instabilities, or proximity to river inflows, may overwhelm the purely Ekman dynamics. For example, comparing cross-shelf frontal movements to those expected from Ekman layer velocities for the coastal current sequence shown in Fig. 9 shows that the Ekman flow estimates are too small by an order of magnitude.

Isopycnal slopes from the coastal currents have the highest correlation with the wind stress over an exponential decay of 4 days. This result contrasts with observations of coastal upwelling during the summer, from Austin and Barth (2002b), who found a relation to be of 8 days. This is related to the changes in the wind field, which during fall and winter are variable on shorter time scales than during spring and summer.

All of our results were focused on times when the freshwater was found trapped to the coast, which in this case it is assumed that the fronts are coastal currents geostrophically balanced in the cross-shelf direction. It is known, however, that periods of sustained upwelling-favorable winds can advect the plume surface waters offshore and eventually detach the plume from the coast (Fong and Geyer 2001), leading to a breakdown of the geostrophic balance. Pimenta and Kirwan (2014) developed an index Γ that quantifies the upwelling efficiency in flushing the plume waters offshore:

$$\Gamma = \frac{A_{\mathrm{Ek}}}{A_p} = \frac{\int_0^t |\tau_o^y/\rho f|\, dx}{A_p}, \tag{11}$$

where A_{Ek} is the cumulative offshore Ekman transport, and A_p is the plume cross-sectional area. They found that for $\Gamma > 1$, the freshwaters are exported offshore.

An estimate of the efficiency of the wind field off the Oregon coast in detaching the coastal current from the coast can be done by calculating Eq. (11), using the wind stress time series presented in Fig. 5 during fall/winter (downwelling season) and the area of the coastal current, approximated by $A_p = (W_p \times h_p)/2$. Using 10 km for W_p and 15 m for h_p (Fig. 7), and integrating the wind stress between zero crossings, 182 wind reversals from downwelling- to upwelling-favorable are found during the six seasons (between 2006 and 2012), roughly five reversals per month; however, only 14 were found in which $\Gamma > 1$, leading to about one reversal every 2 months that are actually capable of completely detaching the plume from the coast.

Based on the index Γ by Pimenta and Kirwan (2014), the coastal current observed off Newport, Oregon, is therefore expected to be a quasi-permanent feature during the fall/winter. Note that Γ even overestimates the detachment, since upwelling winds also cause significant entrainment of ambient waters into the plume. Following Lentz (2004), this can be modeled as $A_e = A_0(1 + t/t_e)$, where A_e is the plume area as a function of time, A_0 is the initial cross-sectional area before the onset of the wind forcing $A_0 = A_p(t = 0)$, $t_e = 2A_0/(\sqrt{Ri_c \rho f/\tau_s})$ is the time it takes for the entrainment to double the initial cross-sectional area of the plume, and Ri_c is a critical Richardson number. Pimenta and Kirwan (2014) have also created an index that incorporated the entrainment, given by $\Gamma_e = A_{\mathrm{Ek}}/A_e$; however, we have chosen to use Γ instead since we are using typical values

for W_p and h_p from in situ data, which inherently contains entrainment.

Despite the fact that upwelling-favorable wind events are in general not capable of detaching the plume from the coast, the wind's role in mixing and entrainment is of extreme importance (e.g., Fong and Geyer 2001; Hetland 2005). Besides the wind field, other processes could lead to detachment of the coastal current and enhance mixing, such as flow over variable topography and instabilities (e.g., Pennel et al. 2012), which are three-dimensional in nature and cannot be properly characterized by the available data.

According to the solution for the Rossby adjustment problem, in a 1.5-layer model (Cushman-Roisin and Beckers 2011), in the case of an unbounded, unforced system, the parameter R from our fit should converge to $R \rightarrow (g'H)^{1/2}/f$. The fact that there are spatial constraints imposed by the topography and the coastline, and the intermittent presence of wind forcing, certainly adds higher complexity to the system and cannot simply be ignored. Laboratory models of unforced buoyant gravity currents adjusted under rotation, along a wall, have demonstrated that the total width of the current $W = bL$ scales with the Rossby radius of deformation $L = (g'h)^{1/2}/f$, where h is the depth of the gravity current at the wall, and b is found empirically from experiments, which have demonstrated that b is $O(1)$ (e.g., Griffiths and Hopfinger 1983). In the case of coastal currents with a sloping bottom, the geostrophic adjustment is assumed to occur offshore of the foot of the front h_p, which in this case $W_s \rightarrow (g'h_p)^{1/2}/f$ (e.g., Lentz and Helfrich 2002; Moffat and Lentz 2012).

Our results, however, show that both $R \rightarrow (g'H)^{1/2}/f$ and $W_s \rightarrow (g'h_p)^{1/2}/f$ only when there are moderate downwelling-favorable winds, and for wind stress close to zero or upwelling favorable, those relationships break down. It is important to keep in mind that the comparisons are made with the wind stress filtered using Eq. (4), and especially for values of filtered wind stress close to zero, it is possible that an upwelling event has occurred not long before the front is measured, but does not clearly show in the final filtered product. This reveals an asymmetric response between upwelling- and downwelling-favorable winds and that the coastal current structure is readily modified by even weak upwelling-favorable winds, while downwelling-favorable winds (moderate) tend to reinforce the relationship described above.

c. *Effects on the ocean biogeochemistry*

Finally, the riverine waters that feed the coastal current have distinct biogeochemical properties compared with adjacent coastal waters, and as a consequence, it is possible to observe a relationship between the optical properties of the water column and the coastal current. An example of this is shown in Fig. 14, which demonstrates how color dissolved organic matter (CDOM) and suspended sediment measured with optical light backscatter are correlated with the fresh, low-density waters from the coastal current. This emphasizes the importance of the coastal current, which can potentially be a primary mechanism responsible for the along-shelf transport of nutrients, sediment, plankton, fish, and invertebrate larvae and therefore play a crucial ecological role during fall and winter off the Oregon coast. The buoyancy-driven current also links the estuaries, carrying carbon and iron that is spread over the shelf and influences the ecosystem, not only during fall and winter, but also the following upwelling season (Chase et al. 2007).

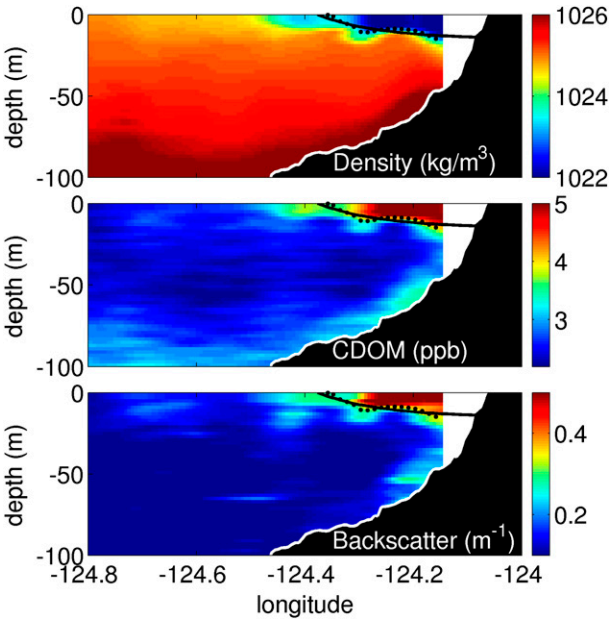

FIG. 14. Observations of (top) cross-shelf density, (middle) CDOM, and (bottom) optical backscatter fields, obtained from a glider survey between 6 and 9 Apr 2007. Discrete position of the front is plotted with dots (only half of the dots were plotted for clarity) and fitted front in solid black line.

5. Conclusions

This work presents the first detailed description of coastal currents observed offshore of central Oregon in fall and winter. Based on a two-layer model, a primary forcing mechanism of these currents is buoyancy, from riverine freshwater discharge into the coastal ocean. The large-scale Davidson Current also contributes significantly to the along-shelf transport, with a smaller contribution by wind forcing. The wind, via cross-shelf Ekman fluxes, significantly impacts the buoyancy front and

current, modifying their geometry and hence velocities and transport. The average transport is 0.08 (±0.07) Sv, and the maximum observed value is 0.49 Sv, magnitudes comparable to the summertime upwelling jet. This persistent buoyancy-driven current may be called the Oregon Coastal Current.

Gliders proved to be a reliable tool to survey the Oregon coast during fall and winter, under harsh weather and oceanic conditions. The present dataset could not have been obtained as effectively using other platforms, for example, ship-based profiling. Even with the limitations of the glider operations in shallow waters over the inner shelf and in the presence of large waves and swift currents, it was possible to characterize the Oregon Coastal Current. The glider data provided the necessary parameters to obtain the coastal current geometry, velocity, and transports.

Several questions still remain unanswered, such as what is the along-shelf spatial coherence of this current, how many rivers contribute to the freshwater transport observed at the NH-line, what is the role of the wind stress in mixing and dispersing this coastal current, under which conditions is the coastal current unstable, does the topography play a significant role in the dynamics of this system, and ultimately what is the fate of the freshwater?

Continuous surveys are of extreme importance in observing and understanding the ocean, and in order to address the questions raised above, in situ data should be collected at more locations along the Oregon coast (and possibly northern California) with proper spatial and temporal resolution. Finally, numerical models that attempt to reproduce fall and wintertime circulation over the Oregon continental shelf must include freshwater input from coastal river discharge and reproduce the Oregon Coastal Current, since it is a persistent, key component of the fall–winter shelf dynamics.

Acknowledgments. P. L. F. Mazzini was supported by the Brazil–U.S. CAPES/Fulbright scholarship. Support for the field work and J. A. Barth, R. K. Shearman, and A. Erofeev was provided by the U.S. National Science Foundation Grants OCE-0527168 and OCE-0961999. We acknowledge the OSU Glider Team for their outstanding, around the clock contributions to making the glider sampling successful. We also thank M. Levine and C. Risien for providing NH-10 mooring data and Captain Mike Kriz and crew of the R/V *Elakha*. We thank Jim Lerczak and Robert Todd for helpful discussions and comments. Finally we would also thank the two anonymous reviewers for their helpful and insightful comments.

APPENDIX A

Transport Derivation

Transports were calculated by integrating the velocities from Eq. (8) over the plume area. The buoyancy-driven transport Q_b was calculated as

$$Q_b = \int\int v_b\, dA = \int_{-W_p}^{-W_b} v_b(x)h(x)\, dx + \int_{-W_b}^{0} v_b(x)h_{\text{topo}}(x)\, dx = \frac{g'H^2}{2f}(1 + e^{-2W_s/R} - 2e^{-W_s/R}), \tag{A1}$$

where the fact that $v_b = 0$ for $x > -W_b$ has been used.

The wind-driven transport was calculated as

$$Q_w = \int\int v_w\, dA = \int_{-W_p}^{-W_b} v_w h(x)\, dx + \int_{-W_b}^{0} v_w h_{\text{topo}}(x)\, dx = v_w\left[H(W_s + Re^{-W_s/R} - R) + \frac{W_b h_p}{2}\right] = \frac{\tau_o^y}{\rho_o r}\left[H(W_s + Re^{-W_s/R} - R) + \frac{W_b h_p}{2}\right], \tag{A2}$$

where $h_{\text{topo}} = (h_p/W_b)x$, assuming a linear bathymetry.

Similarly, the Davidson Current was calculated as

$$Q_D = \int\int v_D\, dA = \int_{-W_p}^{-W_b} v_D h(x)\, dx + \int_{-W_b}^{0} v_D h_{\text{topo}}(x)\, dx = v_D\left[H(W_s + Re^{-W_s/R} - R) + \frac{W_b h_p}{2}\right]. \tag{A3}$$

Finally, the total transport can be found by linearly adding up all of the transports from the three different mechanisms: $Q = Q_b + Q_w + Q_D$.

APPENDIX B

Margules Front Model

For simplicity, the front $h(x)$ can be approximated as a straight interface, the Margules front model (Margules 1906), as has been done in previous plume studies (e.g., Garvine 1999; Fong and Geyer 2002; Lentz and Helfrich 2002). In this case, the coastal current buoyancy-driven velocity can be calculated simply as

$$v_{b_{\text{Margules}}} = \frac{g'h_p}{fW_s}. \tag{B1}$$

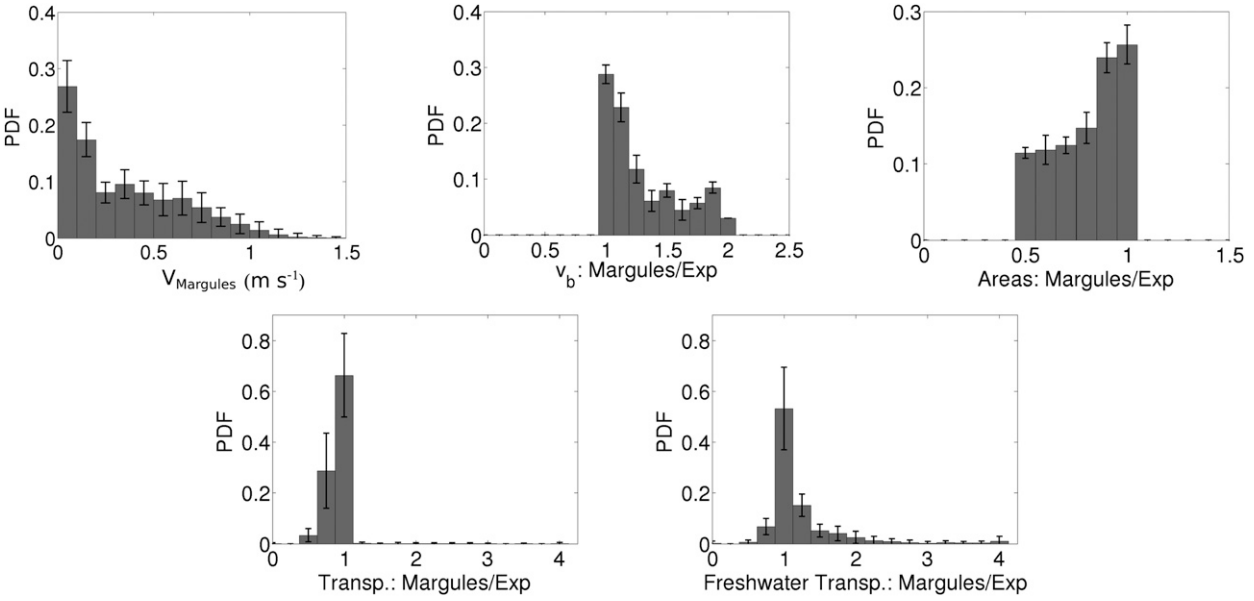

FIG. A1. Probability density functions of (top) Margules-averaged velocities within the (top left) coastal currents, and (top middle) ratios between average buoyancy-driven velocities, and (top right) areas A_s between the Margules front vs the exponential model. Probability density functions of ratios between the Margules front and the exponential model for (bottom left) total transport and (bottom right) freshwater transport. Error bars are standard deviations for each class, obtained from the sensitivity analysis of each fit parameter (W_p, H, and R).

The transport may be obtained by integrating the velocity over the area of the coastal current:

$$\begin{aligned} Q_{b_{\text{Margules}}} &= \int\int v_{b_{\text{Margules}}}\, dA \\ &= \int_{-W_p}^{-W_b} v_{b_{\text{Margules}}} h(x)\, dx + \int_{-W_b}^{0} v_{b_{\text{Margules}}} h_{\text{topo}}(x)\, dx \\ &= \frac{g' h_p^2}{2f}, \end{aligned} \tag{B2}$$

where $h_{\text{topo}}(x)$ is the cross-shelf bathymetry, and the fact that $v_{b_{\text{Margules}}} = 0$ for $x > -W_b$ has been used.

The wind-driven transport was calculated as

$$\begin{aligned} Q_{w_{\text{Margules}}} &= \int\int v_w\, dA = \int_{-W_p}^{-W_b} v_w h(x)\, dx + \int_{-W_b}^{0} v_w h_{\text{topo}}(x)\, dx \\ &= v_w \left(\frac{W_p h_p}{2} \right) \\ &= \frac{\tau_o^y}{\rho_o r} \left(\frac{W_p h_p}{2} \right), \end{aligned} \tag{B3}$$

where $h_{\text{topo}} = (h_p/W_b)x$, assuming a linear bathymetry.

Similarly, the Davidson Current was calculated as

$$\begin{aligned} Q_{D_{\text{Margules}}} &= \int\int v_D\, dA \\ &= \int_{-W_p}^{-W_b} v_D h(x)\, dx + \int_{-W_b}^{0} v_D h_{\text{topo}}(x)\, dx \\ &= v_D \left(\frac{W_p h_p}{2} \right). \end{aligned} \tag{B4}$$

For a Margules front, the total transport (Q_{Margules}) simplifies to

$$\begin{aligned} Q_{\text{Margules}} &= Q_{b_{\text{Margules}}} + Q_{w_{\text{Margules}}} + Q_{D_{\text{Margules}}} \\ &= \frac{g' h_p^2}{2f} + \frac{\tau_o^y}{\rho_o r} \left(\frac{W_p h_p}{2} \right) + v_D \left(\frac{W_p h_p}{2} \right). \end{aligned} \tag{B5}$$

Total velocities within the coastal currents, averaged in the A_s region, are shown in Fig. A1 for the Margules model. Comparing the results from the exponential front (Fig. 12), a slight change is observed for the Margules model, with the 0–0.1 m s^{-1} class reducing to 27%, while increasing the 0.1–0.2 m s^{-1} class to 18%, and it tapers off after reaching 0.7 m s^{-1}, finally nearly vanishing at approximately 1.2 m s^{-1}.

Comparisons between baroclinic velocities and areas for the exponential front versus the Margules model are also shown in Fig. A1. Baroclinic velocities averaged by the area of the plumes are approximately equal in about

30% of cases, and velocities from the Margules model are generally larger than the exponential model, reaching up to twice the latter. The plume areas can be nearly the same in about 20% of the cases, and exponential fronts can have area as much as twice the area of the Margules model.

The ratio of transports estimated from a Margules front model using Eq. (B5) to the exponential front [Eq. (9)] is also shown in Fig. A1. Comparisons between the exponential front versus the Margules model [Eq. (B5)] show that for the total transport the exponential function tends to generate slightly higher transports, about 25% higher for nearly 30% of observations and about 50% higher for roughly 6% of observations. That is a direct result from the exponential fronts having much larger areas, which compensate for larger average velocities attributed to the Margules fronts. For the freshwater transport, the Margules model tends to generate higher transports, 20% higher for about 15% of observations and 50% higher for roughly 5% of observations; however, it can also generate lower transport, about 25% lower for nearly 7% of observations. This arises from the fact that the freshwater content increases toward the coast, and the exponential front model has velocities decreasing toward the coast, while the Margules front velocities are independent of space and dominates the transports over the regions where freshwater is more abundant.

REFERENCES

Allan, J. C., and P. D. Komar, 2006: Climate controls on US West Coast erosion processes. *J. Coastal Res.,* **22,** 511–529, doi:10.2112/03-0108.1.

Allen, J. S., and P. A. Newberger, 1996: Downwelling circulation on the Oregon continental shelf. Part I: Response to idealized forcing. *J. Phys. Oceanogr.,* **26,** 2011–2035, doi:10.1175/1520-0485(1996)026<2011:DCOTOC>2.0.CO;2.

Austin, A. J., and J. A. Barth, 2002a: Drifter behavior on the Oregon–Washington shelf during downwelling-favorable winds. *J. Phys. Oceanogr.,* **32,** 3132–3144, doi:10.1175/1520-0485(2002)032<3132:DBOTOW>2.0.CO;2.

——, and ——, 2002b: Variation in the position of the upwelling front on the Oregon shelf. *J. Geophys. Res.,* **107,** 3180, doi:10.1029/2001JC000858.

Avicola, G., and P. Huq, 2003: The characteristics of the recirculating bulge region in coastal buoyant outflows. *J. Mar. Res.,* **61,** 435–463, doi:10.1357/002224003322384889.

Barnes, C. A., A. C. Duxbury, and B. A. Morse, 1972: Circulation and selected properties of the Columbia River effluent at sea. *The Columbia River Estuary and Adjacent Ocean Waters: Bioenvironmental Studies,* A. T. Pruter and D. L. Alverson, Eds., University of Washington Press, 41–80.

Barnes, S. L., 1994: Applications of the Barnes objective analysis scheme. Part I: Effects of undersampling, wave position, and station randomness. *J. Atmos. Oceanic Technol.,* **11,** 1433–1448, doi:10.1175/1520-0426(1994)011<1433:AOTBOA>2.0.CO;2.

Barth, J. A., and P. A. Wheeler, 2005: Introduction to special section: Coastal advances in shelf transport. *J. Geophys. Res.,* **110,** C10S01, doi:10.1029/2005JC003124.

Blanton, J. O., 1981: Ocean currents along a nearshore frontal zone on the continental shelf of the southeastern United States. *J. Phys. Oceanogr.,* **11,** 1627–1637, doi:10.1175/1520-0485(1981)011<1627:OCAANF>2.0.CO;2.

Chao, S.-Y., 1987: Wind-driven motion near inner shelf fronts. *J. Geophys. Res.,* **92,** 3849–3860, doi:10.1029/JC092iC04p03849.

——, and W. C. Boicourt, 1986: Onset of estuarine plumes. *J. Phys. Oceanogr.,* **16,** 2137–2149, doi:10.1175/1520-0485(1986)016<2137:OOEP>2.0.CO;2.

Chapman, D. C., and S. J. Lentz, 1994: Trapping of a coastal density front by the bottom boundary layer. *J. Phys. Oceanogr.,* **24,** 1464–1479, doi:10.1175/1520-0485(1994)024<1464:TOACDF>2.0.CO;2.

Chase, Z., P. G. Strutton, and B. Hales, 2007: Iron links river runoff and shelf width to phytoplankton biomass along the U.S. West Coast. *Geophys. Res. Lett.,* **34,** L04607, doi:10.1029/2006GL028069.

Cushman-Roisin, B., and J. M. Beckers, 2011: *Introduction to Geophysical Fluid Dynamics: Physical and Numerical Aspects.* 2nd ed. Academic Press, 828 pp.

Eriksen, C. C., T. J. Osse, R. D. Light, T. Wen, T. W. Lehman, P. L. Sabin, J. W. Ballard, and A. M. Chiodi, 2001: Seaglider: A long-range autonomous underwater vehicle for oceanographic research. *IEEE J. Oceanic Eng.,* **26,** 424–436, doi:10.1109/48.972073.

Fong, D. A., and W. R. Geyer, 2001: The response of a river plume during an upwelling favorable wind event. *J. Geophys. Res.,* **106,** 1067–1084, doi:10.1029/2000JC900134.

——, and ——, 2002: The alongshore transport of freshwater in a surface-trapped river plume. *J. Phys. Oceanogr.,* **32,** 957–972, doi:10.1175/1520-0485(2002)032<0957:TATOFI>2.0.CO;2.

——, ——, and R. P. Signell, 1997: The wind-forced response of a buoyant coastal current: Observations of the western Gulf of Maine plume. *J. Mar. Syst.,* **12,** 69–81, doi:10.1016/S0924-7963(96)00089-9.

Garau, B., S. Ruiz, W. G. Zhang, A. Pascual, E. Heslop, J. Kerfoot, and J. Tintore, 2011: Thermal lag correction on Slocum CTD glider data. *J. Atmos. Oceanic Technol.,* **28,** 1065–1071, doi:10.1175/JTECH-D-10-05030.1.

Garcia Berdeal, I., B. M. Hickey, and M. Kawase, 2002: Influence of wind stress and ambient flow on a high discharge river plume. *J. Geophys. Res.,* **107,** 3130, doi:10.1029/2001JC000932.

Garvine, R. W., 1999: Penetration of buoyant coastal discharge onto the continental shelf: A numerical model experiment. *J. Phys. Oceanogr.,* **29,** 1892–1909, doi:10.1175/1520-0485(1999)029<1892:POBCDO>2.0.CO;2.

——, 2004: The vertical structure and subtidal dynamics of the inner shelf off New Jersey. *J. Mar. Res.,* **62,** 337–371, doi:10.1357/0022240041446182.

Gerbi, G. P., R. J. Chant, and J. L. Wilkin, 2013: Breaking surface wave effects on river plume dynamics during upwelling favorable winds. *J. Phys. Oceanogr.,* **43,** 1959–1980, doi:10.1175/JPO-D-12-0185.1.

Grant, W. D., and O. S. Madsen, 1979: Combined wave and current interaction with a rough bottom. *J. Geophys. Res.,* **84,** 1797–1808, doi:10.1029/JC084iC04p01797.

Griffiths, R. W., and E. J. Hopfinger, 1983: Gravity currents moving along a lateral boundary in a rotating frame. *J. Fluid Mech.,* **134,** 357–399, doi:10.1017/S0022112083003407.

Hetland, R. D., 2005: Relating river plume structure to vertical mixing. *J. Phys. Oceanogr.,* **35,** 1667–1688, doi:10.1175/JPO2774.1.

Hickey, B. M., L. J. Pietrafesa, D. A. Jay, and W. C. Boicourt, 1998: The Columbia River plume study: Subtidal variability in the

velocity and salinity fields. *J. Geophys. Res.,* **103,** 10 339–10 368, doi:10.1029/97JC03290.

——, and Coauthors, 2010: River influences on shelf ecosystems: Introduction and synthesis. *J. Geophys. Res.,* **115,** C00B17, doi:10.1029/2009JC005452.

Hill, A. E., 1998: Buoyancy effects in coastal and shelf seas. *The Sea: The Global Coastal Ocean,* A. R. Robinson and K. H. Brink, Eds., *Regional Studies and Syntheses,* Vol. 11, John Wiley and Sons, 63–88.

Huyer, A., 1977: Seasonal variation in temperature, salinity, and density over the continental shelf off Oregon. *Limnol. Oceanogr.,* **22,** 442–453, doi:10.4319/lo.1977.22.3.0442.

——, R. D. Pillsbury, and R. Smith, 1975: Seasonal variation of the alongshore velocity field over the continental shelf off Oregon. *Limnol. Oceanogr.,* **20,** 90–95, doi:10.4319/lo.1975.20.1.0090.

——, R. L. Smith, and E. J. C. Sobey, 1978: Seasonal differences in low-frequency current fluctuations over the Oregon continental shelf. *J. Geophys. Res.,* **83,** 5077–5089, doi:10.1029/JC083iC10p05077.

Jones, E. L., 1918: *The Neglected Waters of the Pacific Coast, Washington, Oregon, and California.* U.S. Coast and Geodetic Survey Series, No. 48, U.S. Government Printing Office, 21 pp.

Large, W. G., and S. Pond, 1981: Open ocean momentum flux measurements in moderate to strong winds. *J. Phys. Oceanogr.,* **11,** 324–336, doi:10.1175/1520-0485(1981)011<0324:OOMFMI>2.0.CO;2.

Lentz, S. J., 2004: The response of buoyant coastal plumes to upwelling-favorable winds. *J. Phys. Oceanogr.,* **34,** 2458–2469, doi:10.1175/JPO2647.1.

——, and C. D. Winant, 1986: Subinertial currents on the southern California shelf. *J. Phys. Oceanogr.,* **16,** 1737–1750, doi:10.1175/1520-0485(1986)016<1737:SCOTSC>2.0.CO;2.

——, and K. R. Helfrich, 2002: Buoyant gravity currents along a sloping bottom in a rotating fluid. *J. Fluid Mech.,* **464,** 251–278, doi:10.1017/S0022112002008868.

——, and J. Largier, 2006: The influence of wind forcing on the Chesapeake Bay buoyant coastal current. *J. Phys. Oceanogr.,* **36,** 1305–1316, doi:10.1175/JPO2909.1.

Margules, M., 1906: Über Temperaturschichtung in stationär bewegter und in ruhender Luft. *Meteor. Z.,* **23,** 243–254.

Matano, R. P., and E. D. Palma, 2010: The upstream spreading of bottom-trapped plumes. *J. Phys. Oceanogr.,* **40,** 1631–1650, doi:10.1175/2010JPO4351.1.

Mazzini, P. L. F., C. Risien, and J. A. Barth, 2011: Observations of anomalous near-surface low-salinity pulses off the central Oregon coast. *Extended Abstracts, 58th Eastern Pacific Ocean Conf.,* South Lake Tahoe, CA, University of California, Santa Cruz. [Available online at http://oceandatacenter.ucsc.edu/EPOC/EPOC2011_ABSTRACTS.pdf.]

Moffat, C., and S. J. Lentz, 2012: On the response of a buoyant plume to downwelling-favorable wind stress. *J. Phys. Oceanogr.,* **42,** 1083–1098, doi:10.1175/JPO-D-11-015.1.

Mork, M., 1981: Circulation phenomena and frontal dynamics of the Norwegian Coastal Current. *Philos. Trans. Roy. Soc.,* **A302,** 635–648, doi:10.1098/rsta.1981.0188.

Münchow, A., and R. Garvine, 1993a: Buoyancy and wind forcing of a coastal current. *J. Mar. Res.,* **51,** 293–322, doi:10.1357/0022240933223747.

——, and ——, 1993b: Dynamical properties of a buoyancy driven coastal current. *J. Geophys. Res.,* **98,** 20 063–20 077, doi:10.1029/93JC02112.

Nash, J. D., and J. N. Moum, 2005: River plumes as a source of large-amplitude internal waves in the coastal ocean. *Nature,* **437,** 400–403, doi:10.1038/nature03936.

Pennel, R., A. Stegner, and K. Branger, 2012: Shelf impact on buoyant coastal current instabilities. *J. Phys. Oceanogr.,* **42,** 39–61, doi:10.1175/JPO-D-11-016.1.

Pierce, S. D., J. A. Barth, R. E. Thomas, and G. W. Fleischer, 2006: Anomalously warm July 2005 in the northern California Current: Historical context and the significance of cumulative wind stress. *Geophys. Res. Lett.,* **33,** L22S04, doi:10.1029/2006GL027149.

Pimenta, F. M., and J. A. D. Kirwan, 2014: The response of large outflows to wind forcing. *Cont. Shelf Res.,* doi:10.1016/j.csr.2013.11.006, in press.

——, ——, and P. Huq, 2011: On the transport of buoyant coastal plumes. *J. Phys. Oceanogr.,* **41,** 620–640, doi:10.1175/2010JPO4473.1.

Royer, T., 1981: Baroclinic transport in the Gulf of Alaska. Part I. Seasonal variations of the Alaska Current. *J. Mar. Res.,* **39,** 239–250.

Schofield, O., and Coauthors, 2007: Slocum gliders: Robust and ready. *J. Field Rob.,* **24,** 473–485, doi:10.1002/rob.20200.

Thomas, A. C., and R. A. Weatherbee, 2006: Satellite-measured temporal variability of the Columbia River plume. *Remote Sens. Environ.,* **100,** 167–178, doi:10.1016/j.rse.2005.10.018.

Whitney, M. M., and R. W. Garvine, 2005: Wind influence on the Delaware buoyant outflow. *J. Geophys. Res.,* **110,** C03014, doi:10.1029/2003JC002261.

Yankovsky, A. E., 2006: On the validity of thermal wind balance in alongshelf currents off the New Jersey coast. *Cont. Shelf Res.,* **26,** 1171–1183, doi:10.1016/j.csr.2006.03.008.